

Calculation of the cyclotron mass and superconducting energy gap as a function of Fermi surface position in zinc*

Philip G. Tomlinson[†]

*Department of Physics, Indiana University, Bloomington, Indiana 47405
and Department of Physics, McMaster University, Hamilton, Ontario, Canada, L8S 4M1*

James C. Swihart

Department of Physics, Indiana University, Bloomington, Indiana 47405

(Received 12 August 1975; revised manuscript received 21 August 1978)

The anisotropic mass enhancement and anisotropic superconducting energy gap are calculated for zinc using pseudopotential theory. The phonon frequencies and polarization vectors are obtained from a model developed here which uses Shaw's optimized model potential with three force-constant terms adjusted to obtain agreement with neutron scattering data. A realistic Fermi-surface geometry is used and the electron wave functions are made up of several orthogonalized plane waves being those obtained by using the Stark and Falicov nonlocal pseudopotential. The band mass and velocities are calculated again using the Stark and Falicov pseudopotential, but with an empirically determined energy dependence of the nonlocal part off of the Fermi surface. With these models, the phonon mass enhancement of the electrons which shows up in the electronic specific heat is calculated, as is the superconducting transition temperature, anisotropic mass enhancement, and the anisotropic superconducting energy gap. The model produces a quasiparticle velocity in good agreement with the magnetic-surface-state measurements of Rahn and Sabo, gives cyclotron resonance masses that agree well with the measurements of Brookbanks, and produces an anisotropy of the energy gap that is in good agreement with the ultrasonic-attenuation measurements of Cleavelin and Marshall. There are other experiments that are not in agreement with the results of this model, but they are not in agreement with the three experiments above, either.

I. INTRODUCTION

The electron-phonon interaction in metals is the interaction responsible for superconductivity. It also produces a phonon cloud around each Bloch electron near the Fermi surface, thus increasing the effective mass of the electron with an observable effect on the measured Azbel'-Kaner cyclotron resonance mass, as well as on the value of the electronic specific heat. In this paper we are concerned with these effects in zinc, and we use pseudopotential theory to carry out realistic calculations.¹ In the following paper² one of us (P. G. T.) uses the same model of the electron-phonon interaction to calculate other observable effects of this interaction in zinc, particularly electron-transport properties such as electrical and thermal conductivity, ultrasonic attenuation, and the electron lifetime due to phonon scattering.

Isotropic effects of the electron-phonon interaction in simple metals such as the specific-heat enhancement and the superconducting transition temperature T_c can be calculated fairly well using rather simple models. This was first shown for the mass enhancement of lead, mercury, and aluminum by Swihart, Scalapino, and Wada,³ and independently for the mass enhancement of lead, aluminum, and sodium by Ashcroft and Wilkins.⁴ Similarly, T_c has been calculated for a number of

simple metals by several groups.⁵⁻⁸ However, any attempt to predict theoretically anisotropic properties such as the mass enhancement or the superconducting energy gap as a function of position on the Fermi surface, or the anisotropic transport properties, must make use of more sophisticated models.

The elements that enter a realistic calculation of electron-phonon interaction effects are (i) the phonon properties, including not only frequency as a function of polarization and wave number, but also the actual polarization vectors of the normal modes, (ii) the geometrical shape of the Fermi surface, (iii) the electron wave function for states on the Fermi surface, (iv) the electronic band velocity at the Fermi surface, and (v) the form of the electron-phonon interaction. For the calculation of isotropic properties the following approximations have been made in the past³⁻⁸: (a) an isotropic or even Debye model is taken for the phonons, (b) the free-electron Fermi sphere is used for the Fermi surface, (c) the electron wave functions are single orthogonalized plane waves (OPW's), (d) the free-electron velocity is taken for the band velocity, and (e) the electron-phonon interaction is treated as a constant.

A few treatments have gone beyond the simplifications discussed above.⁹⁻¹⁹ Calculations were carried out on Pb, Al, K, and Na by Carbotte and

Dynes,⁷ on white tin by Balsley and Swihart,⁹ on aluminum first by Leavens and Carbotte¹⁰ and more recently by Leung¹¹ and by Meador and Lawrence,¹² on potassium by Rice and Sham,¹³ on zinc and thallium by Truant and Carbotte,^{14,15} on zinc and cadmium by Pecheur and Toussaint,¹⁶ and on Be, Mg, and Zn by Borchì *et al.*,¹⁷ in which in each case realistic phonon spectra and electron-phonon interactions appropriate for the particular metal were used. However, except for Refs. 11 and 12, the electron states were treated as consisting of a single OPW on a spherical Fermi surface. Balsley and Swihart did use two-OPW electron states for umklapp scattering. Bennett¹⁸ calculated the anisotropic superconducting energy gap in lead assuming that the anisotropy is due mainly to the anisotropy in the phonon spectrum. He treated the band structure in an approximate way, and concluded that this would have a small effect on the anisotropies in the gap. However, he approximated the electron-phonon interaction by a constant. Klemens, van Baarle, and Gorter¹⁹ calculated the anisotropic electrical conductivity of Sn in which they assumed that the most important contribution to the anisotropy is the anisotropy in the Fermi surface. We shall see that this anisotropy is also important in Zn, but that one can not ignore the other contributions to the anisotropy. Ashcroft and Lawrence²⁰ calculated the anisotropic mass enhancement for indium, in which they also considered the band-structure effects by using realistic electronic wave functions on the true Fermi surface. However, they approximated the phonons by appealing to the properties of phonons in similar metals.

The hexagonal close-packed metal, zinc, was chosen for this study because its structure provides several interesting anisotropic properties, while complications introduced by Fermi-surface distortions are not so great as to preclude a realistic treatment of such. The existence of the extremely accurate pseudopotential fit of Stark and Falicov²¹ (SF), which has been used very successfully in previous calculations,^{8,14} was also a factor in the choice of zinc. Finally, there is a sufficient amount of experimental data available with which to compare our results.

Of the previous calculations discussed above, those of Allen and Cohen,⁸ Truant and Carbotte,¹⁴ Pecheur and Toussaint,¹⁶ and Borchì, De Gennaro, and Tasselli¹⁷ were for zinc. Allen and Cohen approximated the Fermi surface by a sphere, the phonon frequencies by an isotropic fit to neutron scattering data, single-particle electron states by a single OPW, and the phonon Brillouin zone by a Debye sphere. They obtained excellent agreement between their calculated mass-renormalization

parameter λ ($1 + \lambda$ is the mass-enhancement factor due to phonons) using the SF pseudopotential and the λ extracted from the electronic specific-heat coefficient and superconducting transition temperature. The same calculation using the Animalu-Heine²² model potential yielded a value of λ about 36% lower than the experimental values. Their results for the room-temperature electrical resistivity were low by about 50% and 75% for the SF and Animalu-Heine²² potentials, respectively.

Truant and Carbotte¹⁴ made the same assumptions as Allen and Cohen, except that they used a force-constant fit to neutron diffraction data for the phonon model. With this, Truant and Carbotte calculated many anisotropic properties as well as the isotropic ones. Their results for the isotropic mass-enhancement parameter and electrical resistivity were both in very good agreement with experiment. They explored the sensitivity of the results to different force-constant fits, and found that λ is very sensitive to these variations. Since that calculation, phonon data²³ have become available at more points in the Brillouin zone. These neutron data are in best agreement with the force-constant fit which gave the worst results for most of Truant and Carbotte's calculations.

Pecheur and Toussaint¹⁶ used a model similar to that of Truant and Carbotte,¹⁴ and with this they calculated the anisotropic electrical resistivity and the thermal conductivity of zinc as a function of temperature. It should again be emphasized that these authors approximated the electron states by single OPW's on a spherical Fermi surface. Borchì, De Gennaro, and Tasselli¹⁷ had earlier carried out a calculation similar to that of Pecheur and Toussaint, but only for the isotropic electrical resistivity of zinc.

A recent paper by Auluck²⁴ also considers the theory of the anisotropic cyclotron mass and anisotropic superconducting energy gap in zinc. In this work he uses the anisotropic band mass determined by Stark and Auluck²⁵ in a separate calculation in which they used a modified Stark and Falicov pseudopotential. Auluck then compares the band mass averaged over various cyclotron orbits with experimentally determined cyclotron masses to determine the phonon mass-enhancement factor averaged over the same orbit. Arguing that the magnitude of the superconducting energy gap is closely related to the mass enhancement at the same point on the Fermi surface, Auluck then does an approximate calculation for the anisotropic energy gap.

Our paper differs from Auluck's in the important respect that we calculate the anisotropic mass enhancement and energy gap from our models of the phonons, electrons, and electron-phonon interac-

tions. We compare our results with the cyclotron resonance experiments—we do not use these experiments to determine the mass enhancement. Later we shall have more to say about the Stark and Auluck (SA) pseudopotential and the Auluck calculation.

In this paper we present the results of calculations which take into account, we believe, for the first time¹ for a simple metal all five elements listed above which are required for a realistic accounting of electron-phonon interaction effects. A somewhat similar calculation has been carried out for the transition-metal copper by Nowak²⁶ and also by Das.²⁷ We find for the case of zinc, as Nowak and Das found for copper, that all five elements have important effects on the anisotropic electron-phonon properties. This was also found by Leung¹¹ and by Meador and Lawrence¹² in their recent calculations for Al.

Atomic units, $m = \hbar = |e| = 1$, are used throughout. The unit of energy is the double rydberg (27.2 eV). Hexagonal notation is used for reciprocal-lattice vectors. That is, a $(h, k, h' + k', l)$ -type

reciprocal-lattice vector is the vector $h\vec{A} + k\vec{B} + l\vec{C}$ in reciprocal space, where \vec{A} and \vec{B} are primitive reciprocal-lattice vectors that lie in the hexagonal plane and \vec{C} is perpendicular to \vec{A} and \vec{B} . When polar coordinates are used, θ is the angle with the [0001] direction and ϕ is the angle with the [11 $\bar{2}$ 0] direction (i.e., the angle in the base plane with the ΓKHA plane in reciprocal space).

Zinc is a nonideal hcp structure with two atoms per unit cell. The low-temperature interatomic distance in the hexagonal plane is $a = 2.6596 \text{ \AA}$, while the height of the unit cell (twice the distance between planes) is $c = 4.8618 \text{ \AA}$. Figure 1 is a diagram of the first Brillouin zone for zinc with the major symmetry points labeled. The x axis is the $\langle 11\bar{2}0 \rangle$ direction in real space, i.e., the direction for $\phi = 0$ in the basal plane.

In Sec. II we set up the lattice model from which the phonon frequencies and polarization vectors are obtained. In Sec. III we discuss the band-structure effects. In Sec. IV we consider the electron-phonon interaction, and we discuss the calculation of the anisotropic and Fermi sphere average α^2F . The results of the calculation of the anisotropic phonon mass enhancement of the electrons and the anisotropic superconducting energy gap are presented in Sec. V. In Sec. VI we calculate the cyclotron resonance masses for a number of cyclotron orbits and compare with experiments, while in Sec. VII we discuss the superconducting transition temperature and summarize our results.

II. LATTICE DYNAMICS

A realistic calculation of electron-phonon effects in metals requires a phonon model which provides at an arbitrary point \vec{q} in the Brillouin-zone $3n$ frequencies $\omega_{\vec{q}, \lambda}$ and $3n$ polarization vectors $\vec{\epsilon}_{\vec{q}, \lambda}$, where n is the number of atoms per unit cell and λ specifies the particular phonon mode. In order to calculate anisotropic effects, one must consider the full anisotropy of the phonons. An ideal model would realistically treat the long-range interionic forces and correctly predict the frequencies and polarization vectors measured by inelastic neutron scattering.^{23, 28}

Pseudopotential theory provides the promise for such a model,²⁹ but it is not always possible to find a pseudopotential whose predicted phonons agree with the experimental data. A Born-von Kármán force-constant model, on the other hand, can sometimes be fit very accurately to the existing data, but to obtain a good fit for metals it is usually necessary to take into account the forces between ions far removed from each other. Another point is that force constants are less fundamental than pseudopotentials. The forces are parameters

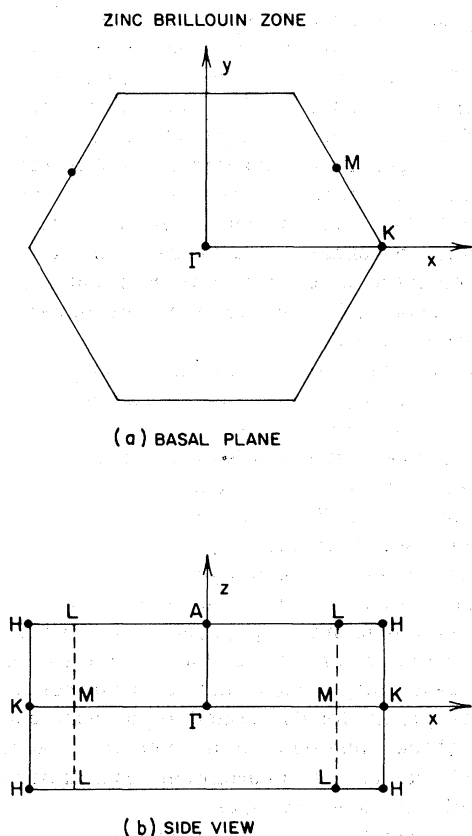


FIG. 1. First Brillouin zone of zinc showing the labels for the major symmetry points and their relation to the Cartesian axes used in this paper.

that are adjusted to give the right phonon spectrum, whereas in the case of, e.g., Shaw's optimized model potential³⁰ (SOMP) the parameters are adjusted to give the right ionic spectra. There also remains the problem of uniqueness in that different fits of the force-constant model may agree with measured phonon frequencies (usually measured only along certain symmetry directions), but give different frequencies in remote regions of the Brillouin zone where measurements have not been taken,¹⁵ or generate different polarization vectors.²⁸

We found that the most satisfactory model for zinc is a pseudopotential model based on SOMP similar to that of Gilat, Rizzi, and Cubiotti³¹ (GRC), but with small corrections added to the dynamical matrix in the form of force constants.

The phonon frequencies and polarization vectors for a given wave vector \vec{q} in the first Brillouin zone are determined by solving an eigenvalue equation,

$$\omega_{\vec{q}\lambda}^2 \epsilon_{\alpha}^{\lambda}(\vec{q}, m) = \sum_{\beta m'} D_{\alpha\beta}(\vec{q}, mm') \epsilon_{\beta}^{\lambda}(\vec{q}, m'), \quad (1)$$

where $\epsilon_{\alpha}^{\lambda}(\vec{q}, m)$ is the α th Cartesian component ($\alpha=1-3$) of the polarization vector for the m th atom in the unit cell and for the λ th mode (i.e., polarization). For zinc, m runs from 1 to 2, corresponding to the two ions per unit cell. For such a case, there are $2 \times 3 = 6$ polarizations or values of λ for each value of \vec{q} . $\omega_{\vec{q}\lambda}$ is the frequency for the mode λ , while $D_{\alpha\beta}(\vec{q}, mm')$ is the $\alpha\beta$, mm' component of the dynamical matrix. The exact nature of the ion-ion forces is contained in the dynamical matrix, while the precise form of the dynamical matrix for a given set of forces depends on the definition of the normal mode. We use a convention in which

$$u_{\alpha}(l, m, t) = (A/\sqrt{MN}) \epsilon_{\alpha}^{\lambda}(\vec{q}, m) \times \exp\{i[\vec{q} \cdot (\vec{X}_l + \vec{\rho}_m) - \omega_{\vec{q}\lambda} t]\}, \quad (2)$$

where $u_{\alpha}(l, m, t)$ is the α th component of the displacement of the m th ion in the l th cell from its equilibrium position as a function of time t when the crystal is vibrating with amplitude A in the normal mode λ with wave vector \vec{q} . Here \vec{X}_l is the position of the lattice point of the l th cell, while $\vec{\rho}_m$ is the equilibrium position of the m th ion in the cell relative to the lattice point of the cell. M is the mass of an ion (all the ions have the same mass) and N is the number of cells in the crystal.

In pseudopotential theory the dynamical matrix is made up of the sum of three terms, each arising from one of three terms in the potential energy which, in turn, is a function of the ion positions:

$$\underline{D}(q) = \underline{D}^R + \underline{D}^C + \underline{D}^E, \quad (3)$$

where \underline{D}^R is from the ion-ion repulsive energy due to core-core overlap, \underline{D}^C is from the Coulomb repulsive energy of interaction between ions, and \underline{D}^E is the conduction-electron contribution. The core radius in a simple metal such as zinc is small compared to ion-ion distances, so, similarly to other work,³¹ we ignore the contribution \underline{D}^R .

\underline{D}^C is computed by the method of Kellermann³² for determining the potential energy of a lattice of point charges. It should be noted that the charge on each ion is taken to be not Z in atomic units, where Z is the valence (in the case of zinc $Z=2$), but rather the charge is Z^* , with $Z^*=2.1461$. This effective valence for the ions arises from the fact that with the use of pseudopotential theory for the calculation of the electronic part \underline{D}^E a depletion or orthogonalization hole charge develops about each ion. To be consistent, the same change of ionic charge must be considered in the calculation of \underline{D}^C .

The electronic contribution \underline{D}^E is determined by pseudopotential theory—in our case, by using SOMP—in which the electronic energy is calculated to second order in perturbation theory. The second-order contribution to the energy by the electrons is²⁹

$$E = \sum_{\vec{q} \neq 0} |S(\vec{q})|^2 F(\vec{q}), \quad (4)$$

where

$$S(\vec{q}) = \frac{1}{mN} \sum_i e^{-i\vec{q} \cdot \vec{R}_i} \quad (5)$$

is the structure factor, and

$$F(\vec{q}) = \frac{\Omega_0}{4\pi^3} \left(\int_{|\vec{k}| \leq k_F^0} d^3k \frac{w(\vec{k}, \vec{q})^2}{\frac{1}{2}(k^2 - |\vec{k} + \vec{q}|)^2} \right) - (\Omega_0 q^2 / 8\pi) |w_{sc}(\vec{q})|^2 \quad (6)$$

is the energy-wave-number characteristic. In the structure factor (5), the sum is over all ion sites with the instantaneous position of the i th ion being \vec{R}_i , n is the number of ions per unit cell (two for zinc), while N is the number of cells in the crystal (of volume Ω). Ω_0 is the volume per ion so that $\Omega = nN\Omega_0$. In carrying out the integration in Eq. (6), we assume that k_F^0 is independent of direction, i.e., k_F^0 is taken as the radius of the free-electron sphere. $w(\vec{k}, \vec{q})$ and $w_{sc}(\vec{q})$ are the screened form factor and the electron screening field, respectively. Screening is handled through the use of the Hartree dielectric function which is used to construct a self-consistent screening potential. For details including the mathematical expressions, see GRC.

GRC, using this model for zinc, found imagin-

TABLE I. Parameters used in Shaw's optimized model potential (SOMP) (Ref. 30) for the phonon model.

Ω_0 (a_0^3)	k_F (a_0^{-1})	Z^*	$A_0(\epsilon_F)$ (double Ry)	$A_1(\epsilon_F)$ (double Ry)	$A_2(\epsilon_F)$ (double Ry)	$\frac{\partial A_0}{\partial \epsilon} \Big _{\epsilon_F}$	$\frac{\partial A_1}{\partial \epsilon} \Big _{\epsilon_F}$	$\frac{\partial A_2}{\partial \epsilon} \Big _{\epsilon_F}$
102.16	0.8338	2.1461	0.984	1.380	0.860	-0.355	-0.484	0.0

ary frequencies near the Γ point ($\vec{q}=0$). On repeating this calculation, we found the same dispersion curves as GRC, except that we did not find imaginary frequencies. We then obtained GRC's calculated energy-wave-number characteristic from Gilat (whom we wish to thank for sending these to us), and, using a linear interpolation between the calculated points in their table, we obtained the same imaginary frequencies as they did. However, using a second-order spline interpolation with their table, we found that the imaginary frequencies disappeared. This shows the extreme sensitivity of imaginary frequencies at low- \vec{q} values to the exact form of the energy-wave-number characteristic.

GRC also explored the effect of the effective mass on phonon dispersion curves and found it to be significant. They suggested that m^* may be used as an adjustable parameter possibility to include some band-structure effects. Our best fit occurs with $m^*=1.1$.

Despite the fact that the imaginary frequencies do not seem to be a problem with the GRC model for zinc, it still is not a satisfactory model for our purposes. The frequencies near $\vec{q}=0$ are not imaginary, but neither do they agree with the elastic constants. More importantly, the frequencies of the low-lying modes in the regions of \vec{q} space where the frequencies are nearly constant with \vec{q} do not agree quantitatively with the neutron scattering data.²³ It is just these phonons that determine the lowest energy peaks in the phonon density of states, and thus have the biggest effect on the electronic properties such as T_c and the mass enhancement.

Brovman, Kagan, and Kholas³³ have investigated the effect of third- and higher-order powers of the pseudopotential on the electronic contribution to the dynamical matrix. They conclude that the highest-order terms give rise to a short-range interaction that is covalent in its structure and that this additional force can be adequately represented by a few force constants. In view of this, we have added three force constants to the dynamical matrix. These affect only the dynamical-matrix elements $D_{zz}(\vec{q}, 11)$ and $D_{zz}(\vec{q}, 12)$, and are included in the framework of the model of DeWames, Wolf-

ram, and Lehman.³⁴ According to their notation, the force constants are

$$\epsilon_{1z} = -1180 \text{ (dyne/cm)},$$

$$\epsilon_{3z} = 785 \text{ (dyne/cm)},$$

$$\beta_{4z} = 246 \text{ (dyne/cm)}.$$

Table I gives the other parameters used in our phonon model. Here A_i , $i=0-2$, is the depth of the SOMP well in double rydbergs for the s , p , and d contributions, respectively. Figure 2 shows

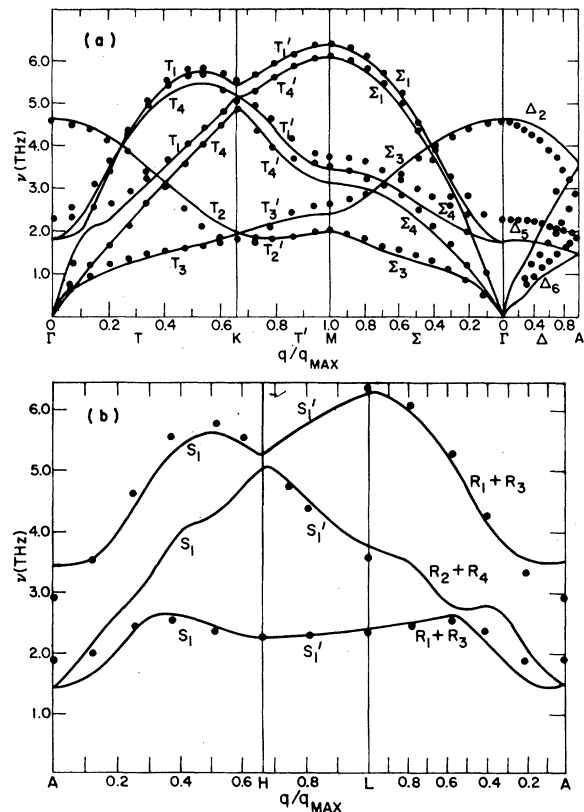


FIG. 2. Phonon dispersion curves, frequency vs wave number, calculated using Shaw's optimized model potential with three added force constants (solid curves) plotted in major symmetry directions. Experimental data of Ref. 23 are shown by the solid dots. (a) \vec{q} in the basal plane and along the c axis; (b) \vec{q} along the upper hexagonal boundary of the Brillouin zone.

the data of Ref. 23 along with our calculated frequencies. The least agreement is near point A, but being along the c axis this point has little statistical weight compared to points off the c axis when integrations are performed over the phonons. This is because the volume of a cylindrical shell of radius r about the c axis increases as $2\pi r$.

In general, the dynamical matrix and polarization vectors are complex, but to simplify diagonalization the dynamical matrix can be made real by a unitary transformation. For two atoms per unit cell the dynamical matrix is of the form

$$\underline{D} = \begin{pmatrix} \underline{D}_{11} & \underline{D}_{12} \\ \underline{D}_{12}^* & \underline{D}_{11} \end{pmatrix}, \quad (7)$$

where the \underline{D}_{ij} are 3×3 matrices which contain the indices of the Cartesian coordinates. We deal with the transformed matrix

$$\bar{D} = \underline{U} \underline{D} \underline{U}^{-1} = \frac{1}{\sqrt{2}} \begin{pmatrix} 1 & i \\ +i & 1 \end{pmatrix} \begin{pmatrix} \underline{D}_{11} & \underline{D}_{12} \\ \underline{D}_{12}^* & \underline{D}_{11} \end{pmatrix} \frac{1}{\sqrt{2}} \begin{pmatrix} 1 & -i \\ -i & 1 \end{pmatrix}, \quad (8)$$

which is real since \underline{D}_{11} is real. Since we apply the calculated phonon polarization vectors only to the calculation of the electron-phonon interaction (see Sec. IV), it is not necessary to carry out the inverse to the transformation (8) on the polarization vectors.

If the dynamical matrix were evaluated and diagonalized each time phonon frequencies and polarization vectors were required in the calculations to be described, the process would have to be performed hundreds of thousands of times. This was avoided by using a modification of the QUAD program written by Mueller *et al.*³⁵ for interpolating electronic band structure. The program had to be modified to apply it to the hcp structure, and also to apply it to phonon frequencies and polarization vectors. It divides the irreducible wedge of the Brillouin zone into a number of cells of equal volume and like shape, and the dynamical matrix is evaluated and diagonalized at each of 27 points in each cell. Then a quadratic least-squares interpolation is performed for each of the six frequencies and each of the six components of the six polarization vectors in each cell, and the interpolated polarization vectors are renormalized.

The error in the fit for the frequencies is much less than the discrepancy between the model and experiment. The polarization vectors present more of a problem in that quadratic interpolation is inadequate in cells in which phonon dispersion curves appear to cross or change character. The adequacy of the interpolation for both frequencies and polarization vectors was tested by calculating

$\alpha^2 F(\cos\theta=1, \phi=0, \omega)$ (see Sec. IV for a discussion of the $\alpha^2 F$ functions) for two cases in which the irreducible wedge was divided into 80 and 252 cells, respectively. The difference between the results of the two calculations was much less than the statistical error inherent in the Monte Carlo integration. The bulk of the remaining calculations were formed with 150 cells in the QUAD³⁵ program. The frequencies of phonons of very small wave vector ($q \leq 0.1q_{\max}$) were approximated by a linear function of q . In the above, q_{\max} refers to the magnitude of the largest \vec{q} vector in the Brillouin zone.

III. BAND STRUCTURE

There are three distinct ways in which the band structure plays a role in electron-phonon effects. These enter *via* (i) the geometrical shape of the Fermi surface, (ii) the electronic wave function for an electron at the Fermi surface, and (iii) the electron-band velocity at the Fermi surface. The wave function, conveniently expressed in terms of coefficients of plane waves, is required in order to calculate the electron-phonon matrix element between two states at the Fermi surface. By using pseudopotential theory, it is possible to limit oneself to determining only the pseudo-wave-function. This has the advantage that fewer plane waves are needed for the pseudo wave function than for the true wave function.

The shape of the Fermi surface is required in the calculation to determine which wave vectors \vec{k} lie on the Fermi surface. It is also needed as is the band velocity in summing over states at the Fermi surface. These two band-structure properties [(i) and (iii) in the paragraph above] are determined if one knows the band energy as a function of \vec{k} , at least in the vicinity of the Fermi surface.

The band structure is dealt with in this calculation by using pseudopotential theory.

The pseudopotential W is much "weaker" in some sense than the true potential V , so that the pseudo wave vector $\phi_{\vec{k}}$ can be accurately expressed by only a few terms in a plane-wave expansion

$$\phi_{\vec{k}}(\vec{r}) = \frac{1}{\sqrt{\Omega}} \sum_{\vec{G}} a_{\vec{G}}(\vec{k}) e^{i(\vec{k} + \vec{G}) \cdot \vec{r}} \equiv \sum_{\vec{G}} a_{\vec{G}}(\vec{k}) |\vec{k} + \vec{G}\rangle, \quad (9)$$

with \vec{G} a reciprocal-lattice vector and Ω the total volume. Each of the functions in terms of which $\phi_{\vec{k}}$ is expanded in (9) is a plane wave which we shall refer to an orthogonalized plane wave (OPW).

The band energy $\epsilon_{\vec{k}}$ is the same for the pseudo-eigenproblem as for the true eigenproblem. Thus it is not necessary to convert to the true wave function in determining the Fermi surface. Nor is the true wave function required for the band

velocity \vec{v}_b at the Fermi surface, since

$$\vec{v}_b = \vec{\nabla}_{\vec{k}} \epsilon_{\vec{k}} \quad (10)$$

involves only the band energy at and near the Fermi surface. Finally, the calculation of the electron-phonon matrix element for the scattering of an electron from one state \vec{k} to another state \vec{k}' requires only the pseudo wave functions $\varphi_{\vec{k}}$ and $\varphi_{\vec{k}'}$ in the form Eq. (9) according to a theorem of Sham.³⁶ Thus in our actual calculations we confine ourselves to the pseudopotential and pseudo-wave-functions, and it is not necessary to use the true wave function at all.

The Fermi surface is determined in the extended-zone scheme in a given direction \vec{k} by finding the magnitude of \vec{k} that satisfies

$$\begin{aligned} & \sum_{\vec{G}'} (\vec{k} + \vec{G}' | H_p | \vec{k} + \vec{G}') a_{\vec{G}'} \\ &= \frac{1}{2} (\vec{k} + \vec{G})^2 a_{\vec{G}} + \sum_{\vec{G}'} S(\vec{G} - \vec{G}') w(\vec{k} + \vec{G}', \vec{G} - \vec{G}') a_{\vec{G}'} \\ &= \epsilon_F a_{\vec{G}} \end{aligned} \quad (11)$$

for arbitrary reciprocal-lattice vectors \vec{G} , with ϵ_F the Fermi energy which is independent of \vec{G} and the direction of \vec{k} . In (11) the pseudopotential matrix element has been broken up into the pseudopotential w for a single ion (i.e., the form factor) and the structure factor S of Eq. (5). In certain directions, no solutions of (11) exist. For such a case the best value of k is at a Brillouin-zone boundary with k on one side of the boundary giving too small a value for the left side of (11), but with k on the other side giving too large a value. In such a direction the Fermi surface does not exist. It is also possible that more than one value of k could satisfy (11) for a given direction. The latter case does not occur for zinc.

We used the Stark and Falicov (SF)²¹ nonlocal pseudopotential in Eq. (11) in obtaining the Fermi surface for our calculations. We also used the SF value of $\epsilon_F = 0.40025$ a.u. (0.8005 Ry). We dropped the spin-orbit term which modifies the Fermi surface by less than 1%.³⁷ The spin-independent pseudopotential is expressed in the form

$$w(\vec{k}, \vec{q}) = u_L(\vec{q}) + \sum_t v(t) \langle \vec{k} + \vec{q} | t \rangle \langle t | \vec{k} \rangle, \quad (12)$$

where u_L is the local part of the potential and hence independent of \vec{k} , while $|t\rangle$ is a Hartree-Fock-Slater atomic function centered on an atomic site at the origin.³⁸ The index t runs over the occupied core states s , p , and d . The local part u_L is given only for \vec{q} equal to certain reciprocal-lattice vectors (see Table II), while the nonlocal strength $v(t)$ is given for the occupied s , p , and d core orbitals (it is nonvanishing only for the d orbital).

Using the SF pseudopotential (in this work we shall always mean by SF pseudopotential, SF with neglect of spin-orbit terms), we found that by carefully choosing the reciprocal-lattice vectors in the expansion (9), we obtained a Fermi surface with only two to eight terms in the expansion (i.e., only two terms on some parts of the Fermi surface, particularly over the flat part of the lens, but up to eight terms at other parts of the Fermi surface) which duplicates as accurately as does Steenhaut and Goodrich³⁷ the Fermi surface obtained with many more terms (SF used 18–27 terms or OPW's). We have in this way a good representation of the SF Fermi surface in which, in agreement with SF, the "butterflies" and "stars" are missing. The reciprocal-lattice vectors taken in addition to $\vec{G} = 0$ are those corresponding to the Bragg planes closest to the k vector. This same procedure was used in determining the pseudo wave functions for the calculation of the matrix elements. Figure 3 shows two sections through our calculated Fermi volume in both the extended zone scheme and the reduced zone scheme.

The parameters in Table II for the pseudopotential were chosen by SF to obtain the best fit to their experimental de Haas-van Alphen periods. More recent experiments on the radio-frequency size effect in zinc³⁷ indicate that the SF Fermi surface is very close to the actual one. However, these experimental results as well as those of SF give us information only on the geometrical shape of the Fermi surface.

A correct pseudopotential must be both nonlocal and energy dependent. The nonlocal property means that there is a first-order contribution to the energy of the form $\langle \varphi_{\vec{k}} | W \varphi_{\vec{q}} \rangle$ which is dependent on \vec{k} . Thus there is a contribution from this term to the band velocity (10) because of the nonlocal

TABLE II. Parameters used in SF pseudopotential (Ref. 21) for the Fermi-surface calculations. All numbers are in atomic energy units (double Ry).

$\langle 0002 \rangle$	$u_L(G)$ local pseudopotential			$v(t)$ nonlocal pseudopotential		
	$\langle 10\bar{1}0 \rangle$	$\langle 10\bar{1}1 \rangle$	$\langle 10\bar{1}2 \rangle$	$v(s)$	$v(p)$	$v(d)$
+0.0020	+0.0075	+0.01725	+0.0100	0	0	+1.575

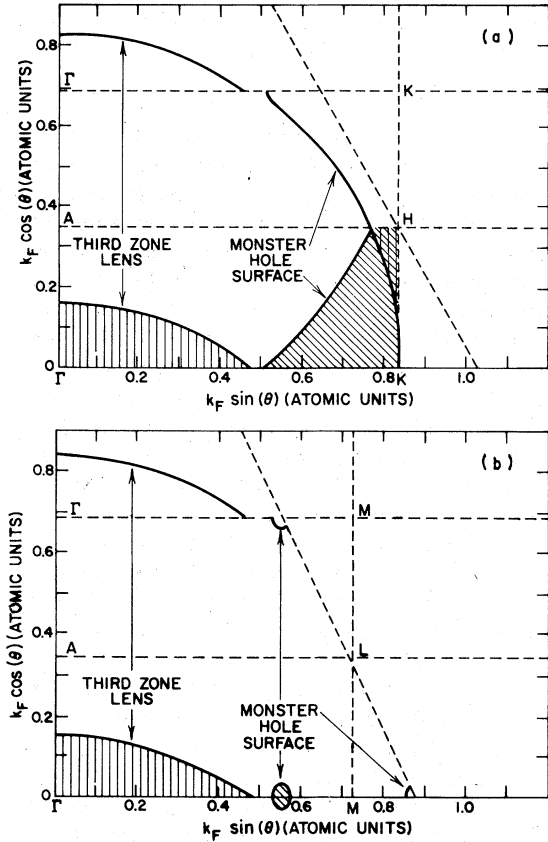


FIG. 3. Fermi surface of Zn using the spin-independent SF pseudopotential and two to six POW's. Both diagrams are for planes in k space containing the c axis. (a) The plane $\phi = 0$ or the $IKHA$ plane; (b) The plane $\phi = 30^\circ$ or the $GLMA$ plane.

property of the pseudopotential. One expects (12) to represent the general form of the pseudopotential where $v(t)$ is the strength of the nonlocal contribution from the t th atomic core state. Since SF fit these strengths empirically, one might reasonably think that the nonlocal part of the SF pseudopotential is essentially correct at least in the neighborhood of the Fermi surface. (Of course there is the highly likely possibility that the SF fit to the data is not unique. In such a case the nonlocal part of the SF pseudopotential may not be correct.)

On the other hand, no energy dependence has been put into the SF pseudopotential since the parameters are fit to the experimental data at just one energy, the Fermi energy. But the energy dependence of the pseudopotential also contributes to the band velocity (10). That is, the right-hand side of (10) at the Fermi surface is the rate that the energy changes as one moves off the surface normal to it. Since, as we have noted, there is a

first-order contribution to the energy of the form $(\phi_{\vec{k}}, W \phi_{\vec{k}})$ the energy dependence of W contributes to the gradient of ϵ with respect to \vec{k} .

One thus sees, by the argument of the paragraph above as well as by the argument that the fit of the parameters in the SF pseudopotential may not be unique, that one can not expect the SF pseudopotential to give the correct band velocity at the Fermi surface. Hence it is not surprising that when one compares the band density of states calculated from the SF pseudopotential, the experimental superconducting transition temperature T_c , and the experimental temperature coefficient γ of the electronic specific heat, one does not get a consistent set of results. We shall now discuss this in detail.

Let us first consider the band density of states normalized to that of the free-electron sphere

$$\rho_b = \frac{n_b(\epsilon_F)}{n_{fe}(\epsilon_F^0)} = \frac{1}{4\pi k_F^0} \int_{FS} \frac{ds}{v_b(\vec{k})}, \quad (13)$$

where n_b is the band density of states for one spin and n_{fe} is the density of states for the free-electron Fermi sphere with ϵ_F^0 the free-electron Fermi energy $\frac{1}{2}(k_F^0)^2$. k_F^0 is the free-electron Fermi wave vector. The integral is over the true Fermi surface. We have found a value of

$$\rho_b = 0.54 \quad (14)$$

using the SF pseudopotential and taking 1200 points on $\frac{1}{24}$ of the zone. (Allen, Cohen, Falicov, and Kasowski⁸ quote a value of 0.59. However, 0.54 seems more consistent with their Fig. 1.)

The electronic specific-heat temperature coefficient γ is related to the band density of states by

$$\gamma = (2\pi^2/3) k_B^2 n_b(\epsilon_F) (1 + \lambda), \quad (15)$$

where k_B is the Boltzmann constant and λ is McMillan's mass-renormalization parameter due to the phonon cloud.³⁹ A value of 0.54 for the normalized density of states together with the experimental value of⁴⁰ $\gamma = 642.5 \pm 1.0 \mu\text{J}/\text{mole K}^2$ in Eq. (15) requires that λ be 0.61. This, in turn, according to McMillan's formula³⁹ would give a superconducting transition temperature T_c greater than 5.0°K compared to the experimental value for zinc⁴¹ of $T_c = 0.85^\circ\text{K}$. On the other hand, if we take McMillan's value of $\lambda = 0.38$ which is obtained from the experimental T_c and use this in (15) together with the experimental γ , we find $\rho_b = 0.63$. Thus we see that the SF band velocity must be modified to agree with experiment. Further this modification can be made *via* the energy dependence of the pseudopotential without changing the geometry of the Fermi surface that this pseudopotential gives.

There are other indications that one should not use the unmodified band velocities from an energy-

independent SF pseudopotential. First, Shaw's optimized model potential³⁰ (SOMP) for zinc gives a value for the k derivative of the diagonal term of

$$\frac{d}{dk} \langle k | W_{\text{SOMP}} | k \rangle = 0.037 \quad (16)$$

in atomic units, compared to the SF value of

$$\frac{d}{dk} \langle k | W_{\text{SF}} | k \rangle = 0.16. \quad (17)$$

Equation (16) includes the effect of the energy dependence of SOMP and was calculated from the parameters for Zn given in Ref. 31.

One can use the local on-the-Fermi-surface version of the SF pseudopotential (\vec{k} and \vec{k}' lying on the Fermi sphere, thus suppressing all but the \vec{q} dependence) and calculate v_b at each point on the SF Fermi surface. Then one can correct for the nonlocality and energy dependence by adding the value of Eq. (16) to the local velocity. If, instead, we would add Eq. (17) to the local velocity we would have the unmodified SF band velocity with the effect of nonlocality approximately included, but with no energy dependence of the pseudopotential included.

If this modified band velocity, obtained using Eq. (16) together with the on-the-Fermi-surface local version of the SF pseudopotential, is used in Eq. (13) and the integration is still over the SF Fermi surface, one obtains $\rho_b = 0.615$, which is in reasonable agreement with the specific heat and T_c data.

Stark and Auluck²⁵ and also Moriarty⁴² are in agreement with our conclusion that the unmodified SF band velocity is too large. Both of these groups were concerned with the effects of the d band but approached the problem in quite different ways. Although Stark and Auluck find the same band density of states with the SF pseudopotential as did Allen *et al.*⁸ (one can see this from Auluck's²⁴ Table II, in which he gives 0.42 for the enhancement factor λ from specific heat with the SF model), they find with their modified pseudopotential (their SA model) a smaller λ from specific heat. This means that ρ_b must be larger for their SA model than for the SF model. But Auluck states that the SA model gives the same Fermi surface as the SF model. Hence their SA model must give, at least on the average, a smaller band velocity. Moriarty concludes a similar result in which he finds for his nonlocal pseudopotential that the k derivative of the diagonal matrix element of the pseudopotential at the Fermi surface [corresponding to Eqs. (16) and (17)] has the value 0.045 in double rydberg atomic units. This is fairly close to the value of Eq. (16), which we had concluded

was a reasonable value before becoming aware of Moriarty's work. It is not close to the unmodified SF value of Eq. (17).

The band velocity is required in only two places in our calculations—for the density of states in integrations over the Fermi surface and for calculations of cyclotron masses in integrations over cyclotron orbits. For integrations over the Fermi surface we first used a local version of the SF pseudopotential to calculate the band velocity at each point on the Fermi surface. That is, for a given point on the Fermi surface we calculated the values of the relevant plane-wave matrix elements to determine the band energy using the unmodified nonlocal SF pseudopotential. We then calculated new band energies for new k values slightly below and slightly above the Fermi surface and on the normal through the point. In these last calculations the same values were taken for the matrix elements of the pseudopotential as for the calculation of the energy on the Fermi surface. In this sense the pseudopotential is treated as a local potential. This variation of the band energy with the normal component of the k vector then determines the local potential band velocity.

This local potential band velocity gives a value of $\rho_b = 0.625$ for the calculation of the band density of states. This same band velocity was used in the density of states for all integrations over the Fermi surface. Then the result was multiplied by the factor 0.615/0.625 to correct for the nonlocality and energy dependence of the pseudopotential.

For the cyclotron orbits, more care was taken. The band velocity was determined by

$$\vec{v}_b(\vec{k}) = [\vec{\nabla}_{\vec{k}}^0 + \alpha(\vec{\nabla}_{\vec{k}} - \vec{\nabla}_{\vec{k}}^0)] \epsilon_{\vec{k}}, \quad (18)$$

where $\vec{\nabla}_{\vec{k}}^0$ denotes differentiation in which the pseudopotential is not allowed to vary with \vec{k} . That is, this operator operating on $\epsilon_{\vec{k}}$ gives the local SF band velocity as discussed in the preceding two paragraphs. The constant α is treated as an adjustable parameter to obtain the best fit with the experimental cyclotron mass data. In order to get the same derivative of the diagonal matrix element as in Eq. (16), we would use a value of $\alpha = 0.037/0.16 = 0.23$. However, as we shall see, we obtained better fits with $\alpha \approx 0.45$.

The result of such a calculation with $\alpha = 0.45$ on the lens is shown in Fig. 4. Plotted here is the magnitude of the band velocity together with the magnitudes of the components parallel and perpendicular to the c axis, all normalized to the magnitude of the free-electron velocity on the Fermi sphere. Note that at the top of the lens ($\theta = 0$), where the wave function is very nearly free-electron-like, the unmodified SF band velocity is about 1.1 (as given by the dashed curve),

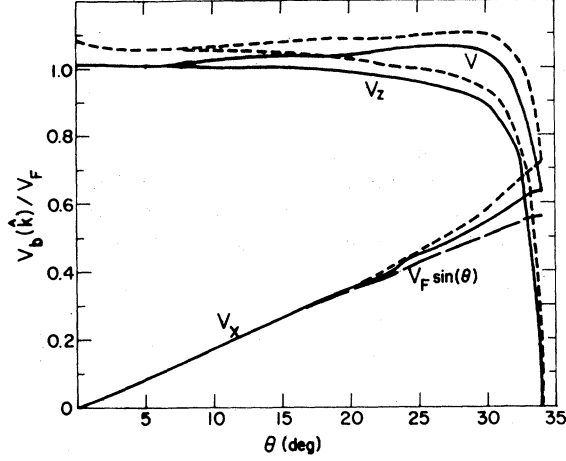


FIG. 4. Magnitude v_b of the band velocity on the lens together with the components v_z parallel to the c axis and v_x perpendicular to the c axis. The velocities are normalized with respect to the free-electron Fermi velocity v_F and are given as a function of the angle θ of k_F with the c axis in the extended-zone scheme. The dashed curves (----) are determined using the unmodified SF pseudopotential, while the solid curves (—) are from the modified SF pseudopotential in which the nonlocal contribution is decreased by $\alpha = 0.45$ in Eq. (18). Also plotted as a comparison to v_x is $v_F \sin \theta$ (---).

which is approximately 10% larger than the free-electron value. This difference is due almost entirely to the nonlocality of the SF pseudopotential. Thus when the nonlocal contribution is partially canceled by the energy-dependent contribution by $\alpha = 0.45$ in Eq. (18), the band velocity then becomes nearly that of the free electron. This is seen in Fig. 4, in which the normalized velocity is approximately unity for the solid curve at small values of θ .

IV. ELECTRON-PHONON INTERACTION

As shown by Sham,³⁶ the matrix element $g_{\vec{k}'\vec{k}\lambda}$ for the scattering of a Bloch electron from wave vector \vec{k} to \vec{k}' with emission of a phonon of wave vector \vec{q} and polarization λ can be expressed in terms of the corresponding pseudo wave functions $\varphi_{\vec{k}}$ and $\varphi_{\vec{k}'}$, and the pseudopotential $w(\vec{k}, \vec{q} + \vec{G})$ as

$$g_{\vec{k}'\vec{k}\lambda} = \sum_{\vec{G}, \vec{G}'} a_{\vec{G}}(\vec{k}')^* a_{\vec{G}}(\vec{k}) g_{\vec{k}' + \vec{G}', \vec{k} + \vec{G}, \lambda}^{\dagger}, \quad (19)$$

where $a_{\vec{G}}(\vec{k}')$ and $a_{\vec{G}}(\vec{k})$ are the expansion coefficients, as in (9), in terms of OPW's of the pseudo-wave-functions $\varphi_{\vec{k}'}$ and $\varphi_{\vec{k}}$, respectively, and $g_{\vec{k}'\vec{k}\lambda}^{\dagger}$ is the electron-phonon matrix element for the scattering from the one OPW state $|\vec{k}\rangle$ to the one OPW state $|\vec{k}'\rangle$ with the emission of a phonon of wave vector \vec{q} and polarization λ . This one

OPW matrix element is given by

$$g_{\vec{k}'\vec{k}\lambda}^{\dagger} = -i \left(\frac{1}{2NM\omega_{\vec{q}\lambda}} \right)^{1/2} w(\vec{k}, \vec{q} + \vec{G}) \frac{1}{n} \times \sum_m (\vec{G} + \vec{q}) \cdot \vec{\epsilon}^{\lambda}(\vec{q}, m) \exp(-i\vec{G} \cdot \vec{\rho}_m). \quad (20)$$

In Eqs. (19) and (20) \vec{q} is the wave vector $\vec{k} + \vec{G} - \vec{k}' - \vec{G}'$ and $\vec{k} - \vec{k}'$, respectively, in both cases reduced to the first zone. Thus \vec{q} is the same vector in both equations, while \vec{G} in (20) is the reciprocal-lattice vector which reduces $\vec{k} - \vec{k}'$ to the first zone. $\vec{G} = 0$ for a normal scattering process, while $\vec{G} \neq 0$ for an umklapp scattering. As before, N is the number of unit cells in the crystal and $n = 2$ is the number of ions per unit cell. The sum over m goes from unity to two for the two ions.

By using the transformed real dynamical matrix of Eq. (8) to obtain the phonons, we obtain real polarization vectors \vec{f}_1 and \vec{f}_2 related to the complex polarization vectors $\vec{\epsilon}(m)$ by

$$\begin{pmatrix} \vec{f}_1 \\ \vec{f}_2 \end{pmatrix} = U \begin{pmatrix} \vec{\epsilon}_1 \\ \vec{\epsilon}_2 \end{pmatrix}, \quad (21)$$

where U is the unitary transformation matrix in Eq. (8). If we set the origin so that $-\rho_1 = \rho_2 \equiv \rho$, then

$$g_{\vec{k}'\vec{k}\lambda}^{\dagger} = -i \frac{1-i}{\sqrt{2}} \left(\frac{1}{2NM\omega_{\vec{q}\lambda}} \right)^{1/2} w(\vec{k}, \vec{q} + \vec{G}) \frac{1}{2} (\vec{G} + \vec{q}) \times \{ \vec{f}^{\lambda}(\vec{q}, 1) [\cos(\vec{G} \cdot \vec{\rho}) - \sin(\vec{G} \cdot \vec{\rho})] + \vec{f}^{\lambda}(\vec{q}, 2) [\cos(\vec{G} \cdot \vec{\rho}) + \sin(\vec{G} \cdot \vec{\rho})] \}. \quad (22)$$

We shall only need the absolute square $|g_{\vec{k}'\vec{k}\lambda}^{\dagger}|^2$, so the factor $-i(1-i)/\sqrt{2}$ may be dropped and all quantities are real.

The pseudopotential form factor $w(\vec{k}, \vec{q})$ occurs only for \vec{q} equal to reciprocal-lattice vectors for the band-structure problem of Sec. III, and thus could be determined only for these values by Stark and Falicov.²¹ However, for the electron-phonon interaction (20) the form factor must be known for a continuous range of \vec{q} values from zero to slightly more than two times k_F^0 . Hence the SF pseudopotential (12) must be extrapolated to small values of \vec{q} , as well as interpolated to \vec{q} values between reciprocal-lattice values.

We are not concerned with values of q much larger than $2.2 k_F$, since we are only interested in Fermi-surface scattering. It is true that with multi-OPW wave functions on the Fermi surface there are plane-wave components with wave vectors greater than k_F . Hence in the matrix elements there will be plane waves connecting with plane waves with a wave vector difference greater than $2k_F$. However, only those plane waves near

the Fermi sphere occur in the Fermi-surface wave functions with non-negligible coefficients, and thus q values larger than $2.2 k_F$ make very small contributions to the matrix elements.

For the intermediate values of \bar{q} , i.e., those in the range where the SF form factor is known, a spline interpolation of the local part of SF was taken, while the nonlocal part of the SF form factor was considered to be correct over this entire range. For the extrapolation to small \bar{q} vector it is possible to carry out the same procedure as with the interpolation. This was done by Allen *et al.*⁸ and by Truant and Carbotte,¹⁴ in which the SF pseudopotential was smoothly interpolated between the values at the reciprocal-lattice vectors and the limiting value $-\frac{2}{3}\epsilon_F$ at \bar{q} equal to zero for \bar{k} and \bar{k}' on the Fermi sphere. We also used this procedure at first, but with it we obtained a calculated value of λ that was about 30% too low. By the calculated λ , we mean the value obtained using the electron-phonon interaction (19)–(22) with the appropriate integrals over the Fermi surface, as we shall describe below. We do not mean the value of λ obtained from comparing the calculated band density of states with the electronic specific heat, as in Eq. (15).

Another way of extrapolating to small \bar{q} values is to extrapolate the local value of the SF pseudopotential such that the total nonlocal pseudopotential agrees with Shaw's optimized model potential³⁰ (SOMP) for small \bar{q} and for \bar{k} and \bar{k}' on the Fermi sphere. When one uses SOMP including the correction to the effective mass due to the nonlocal and energy-dependent nature of the diagonal term of the pseudopotential,⁴³ one gets a long-wavelength limit significantly different from $-\frac{2}{3}\epsilon_F$. For zinc the appropriate limit is $-\frac{2}{3}(1.23)\epsilon_F$. SOMP calculated in this way does not join smoothly to the fitted points of SF. However, the former potential does have a better theoretical foundation than the extrapolated SF potential at small \bar{q} . Thus we used SOMP with the k -dependent mass for $0 \leq q \leq 1.2k_F$. For larger \bar{q} values we connected with SF by a spline interpolation. With this pseudopotential, which is greater in magnitude for small \bar{q} than the extrapolated SF pseudopotential, the calculated value of λ is 0.36. This value of λ agrees quite well with McMillian's value³⁹ of 0.38.

A third extrapolation that we used consisted of fitting to the nonlocal pseudopotential of Appapillai and Williams⁴⁴ at small values of \bar{q} . Although this pseudopotential goes to the value $-\frac{2}{3}\epsilon_F$ on the Fermi surface for $\bar{q}=0$, and thus is not as strong for small \bar{q} as is the SOMP with the k -dependent effective mass, it does have a larger magnitude in the region of $q/k_F \sim 1$. The value of λ calculated

with this pseudopotential is 0.33, which is about 10% too low. See the following paper,² Fig. 1, for a plot of the two form factors discussed here together with a plot of SOMP with $m^*=1$. The following paper also has a more complete discussion concerning the form factor.

For the physical properties of interest to us in this paper, the electron-phonon interaction enters only through the anisotropic $\alpha^2 F$ function

$$\alpha^2 F(\bar{k}, \omega) = \frac{1}{(2\pi)^3} \int_{\text{FS}} \frac{dS'}{|\bar{v}_b(\bar{k}')|} \sum_{\lambda} |g_{\bar{k}'\bar{k}\lambda}|^2 \delta(\omega - \omega_{\bar{q}\lambda}), \quad (23)$$

and the Fermi-surface average

$$\alpha^2 F(\omega) = \int_{\text{FS}} \frac{dS}{|\bar{v}_b(\bar{k})|} \alpha^2 F(\bar{k}, \omega) / \int_{\text{FS}} \frac{dS}{|\bar{v}_b(\bar{k})|}. \quad (24)$$

For the transport properties, generalizations of $\alpha^2 F$ enter that involve deviations of the electron distribution from the Fermi-Dirac distribution. These functions are discussed in the following paper.² All of these functions involve integrals of the square of the magnitude of the electron-phonon interaction matrix element over the Fermi surface, but with different weighting functions. Thus the calculations of the $\alpha^2 F$ functions were carried out by the same method, namely, a Monte Carlo integration over the Fermi surface, and in fact were frequently done simultaneously.

The $\alpha^2 F$ functions may be thought of as the density of phonon states available to the electron at k :

$$F(\bar{k}, \omega) = \frac{1}{(2\pi)^3} \int_{\text{FS}} \frac{dS'}{|\bar{v}_b(\bar{k}')|} \sum_{\lambda} \delta(\omega - \omega_{\bar{q}\lambda}) \quad (25)$$

weighted by the electron-phonon interaction squared. The method of calculation of the anisotropic $\alpha^2 F$ at a given value of \bar{k} on the Fermi surface was as follows: The free-electron Fermi sphere was divided up by a grid system. A randomly scattered electron state \bar{k}' on the true Fermi surface but within a given grid square in terms of its direction was found by using a random number generator. If the Fermi surface existed in that direction in the extended zone scheme, then that would determine \bar{k}' . If the Fermi surface did not exist, this direction would be discarded and a new random direction would be determined. The phonon \bar{q} vector was determined as $\bar{k}' - \bar{k}$ reduced to the first zone. With our stored information on the electron wave functions at \bar{k} and \bar{k}' together with the phonon frequencies and polarization vectors corresponding to \bar{q} , the electron-phonon interaction Eq. (19) was evaluated for each λ .

The δ function in Eq. (23) was handled by dividing the phonon frequency range into 100 equally

spaced regions or bins. The scattering from \bar{k} to \bar{k}' would then give a contribution to $\alpha^2 F$ at the value of ω corresponding to the bin in which $\omega_{\bar{q}\lambda}$ would fall. The magnitude of the contribution was $\Delta S'$, a Fermi-surface area element, divided by the band velocity times the electron-phonon matrix element squared times the reciprocal of the bin width. For a given \bar{k} and \bar{k}' , all phonon polarizations were used. This process was then first repeated for all the 23 other \bar{k}' points obtained by the point operations of the hexagonal symmetry. Then a new random \bar{k}' was obtained in the next grid square, and so on. For each of the anisotropic $\alpha^2 F$ functions, 6264 \bar{k}' points were taken.

The isotropic $\alpha^2 F$ functions were calculated in a similar way, except that both \bar{k} and \bar{k}' were random points within the grids on the Fermi surface. For these calculations 9216 pairs of \bar{k} and \bar{k}' were taken.

Figures 5–7 are plots of calculated $\alpha^2 F$ functions for zinc. Figure 5 shows our calculated Fermi-surface averaged $\alpha^2 F(\omega)$ of Eq. (24) using the SF pseudopotential extrapolated to Appapillai and Williams at small q . Although this function has been determined from anomalous tunneling data combined with a numerical inversion of the Eliashberg gap equation for a number of strong-coupling

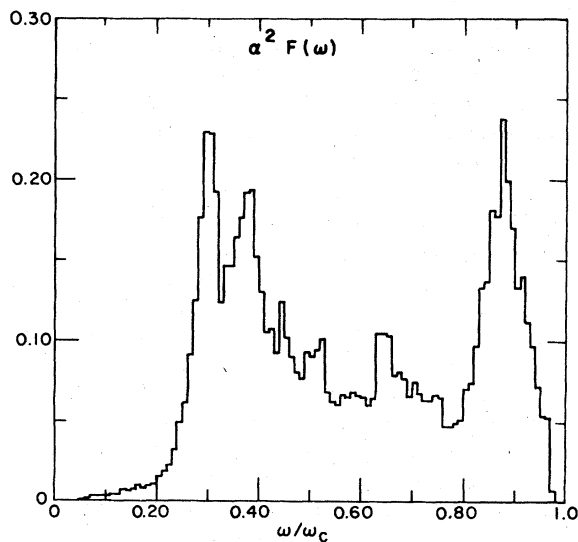


FIG. 5. Isotropic $\alpha^2 F$ as a function of reduced frequency. $\omega_c = 4.178 \cdot 10^{13}$ rad/sec is the maximum phonon frequency. The pseudopotential used in the calculation was SF Ref. 21 extrapolated to Appapillai and Williams (Ref. 44) at small q . The band velocity used in the integral over the Fermi surface was that of the nonlocal SF, but the final integral was multiplied by the factor 0.615/0.54 to correct for the modification of v_b due to the energy dependence of the pseudopotential.

superconductors,⁴⁵ zinc appears to be too weak coupling to make this procedure feasible. Thus there are no data at present with which to compare our calculated $\alpha^2 F$.

Note that there are three large peaks in the calculated $\alpha^2 F$ function at values of ω/ω_c of approximately 0.30, 0.38, and 0.88, corresponding to frequencies of 2.0, 2.5, and 5.9 THz, respectively. There are two smaller peaks at $\omega/\omega_c = 0.50$ and 0.65, corresponding to 3.3 and 4.3 THz, respectively. These peaks also occur at about the same frequencies in $\alpha^2 F$ functions calculated using the SF pseudopotential extrapolated to SOMP at small- q values. In fact, with this latter potential we have calculated the isotropic $\alpha^2 F$ for three cases (not shown here; see Tomlinson's thesis): multi-OPW wave functions on the true Fermi surface, one-OPW wave functions on the true Fermi surface, and one-OPW wave functions on the spherical Fermi surface. In all three calculations there are peaks at approximately these five frequencies, with the ones at ω/ω_c equal to 0.30, 0.38, and 0.88 being the dominant ones. The peaks at ω/ω_c equal to 0.50 and 0.65 are almost lost in

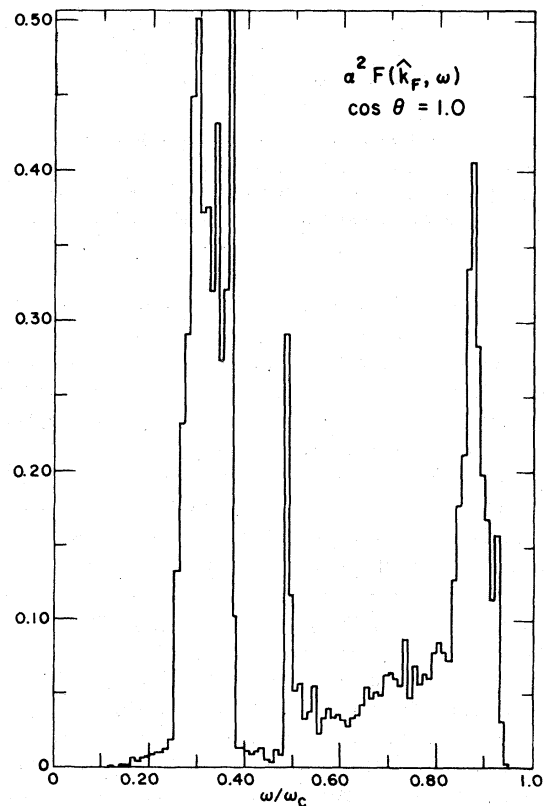


FIG. 6. Anisotropic $\alpha^2 F$ in the direction of the c axis as a function of the frequency. The pseudopotential used was the same as for Fig. 5.

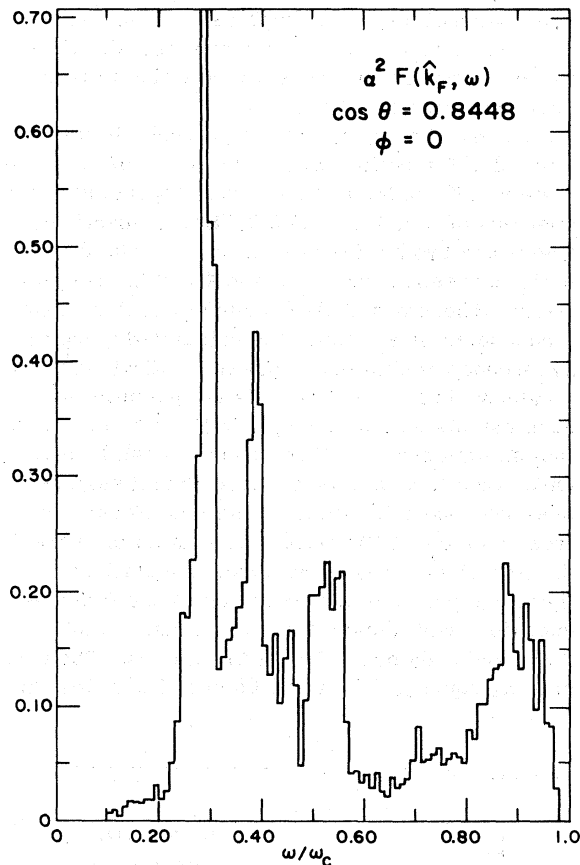


FIG. 7. Anisotropic $\alpha^2 F$ in the direction $\cos\theta = 0.8448$ and $\phi = 0$ as a function of frequency. This direction corresponds to the rim of the lens. The pseudopotential used was the same as for Fig. 5.

the noise in the last two calculations.

Since the main thing that is constant in the four calculations of $\alpha^2 F$ discussed above is the phonon model, we conclude that since the peaks occur at nearly the same frequencies for each calculation, the position of the peaks must reflect the positions of peaks in the phonon density of states F . Also, the three dominant peaks are dominant in all four calculations, while the two minor peaks are minor in all the calculations. So in some gross sense the magnitude of the peaks is also determined by essentially only the phonon density of states. However, for the finer details the other parts of the model play a role. Thus the electron-phonon interaction, the Fermi surface, and the electronic wave functions, i.e., the parts of the model that go into the α^2 of $\alpha^2 F$ are also determining factors in the size and exact location of the peaks. For example, for the one-OPW on the spherical Fermi surface, the peak at $\omega/\omega_c = 0.38$ is larger than the one at 0.30, which is just the reverse of the case

of multi-OPW's on the true Fermi surface in Fig. 5.

On looking at the phonon dispersion curves, Fig. 2, we see that some of the branches are rather constant in frequency in the frequency region near 2 THz and also in the region of 6 THz. However, these curves are only along a few directions in the three-dimensional zone, and thus all such flat regions may not appear in these figures. Furthermore, where they do appear, we cannot tell from the graphs how large the phase space of the flat region is.

Truant and Carbotte¹⁴ have also calculated isotropic $\alpha^2 F$ functions for zinc with single OPW wave functions on a spherical Fermi surface. They used two different models for the phonon spectra (both different from the one used by us). They also find five peaks in both the $\alpha^2 F$ function and in the phonon density of states for both phonon models. Actually, with the one model a small peak in the phonon density of states splits into two small peaks in the $\alpha^2 F$ function. It is of interest to compare the locations of their calculated peaks with ours. In their one model the peaks in $\alpha^2 F$ occur at approximately 1.6, 2.4, 3.6, 4.1, and 5.7 THz, while with the second model they find peaks at 1.9, 3.4, 3.9, and 5.6 THz with the very small double peaks at 2.2 and 2.4 THz. Thus the five peaks occur at roughly the same places for our phonon model and for their two phonon models. We also agree with the models of Truant and Carbotte in that the lowest- and highest-frequency peaks are major ones and in that the third and fourth peaks are minor ones. We disagree that our peak at 2.5 THz is a major one, while with both their models this is a minor peak.

Although there is fair agreement between the results of their two phonon models and our results as to the locations of the peaks in $\alpha^2 F$, it is true that with their one model [they donate it by MEPM (McDonald, Elcombe, and Pryor modified force constants), which they considered to be their better model], the major low-energy peak is 20% lower in energy than is the same peak in our model. This can be attributed to the very low energies of the phonons of the lowest branch in their model in the LH region of the Brillouin zone. More recent neutron data²³ shows that this branch does not have such low energy (see Fig. 2).

We further have general agreement with Truant and Carbotte on the magnitude of the dimensionless quantity $\alpha^2 F$. In all of the calculations it ranges from about 0.05 to 0.15, going over 0.2 only at the major peaks and going under 0.1 only at three valleys in the middle of the frequency range. Such quantitative agreement is possible on comparing calculations using the free-electron spherical

Fermi surface with those using the true Fermi surface only if the results in Eq. (23) of the former are multiplied by ρ_0 of Eq. (13). Truant and Carbotte used this procedure to correct for the actual Fermi-surface density of states when integrating over the free-electron Fermi sphere.

It is gratifying to find such close agreement for the isotropic α^2F obtained with such widely differing models. Thus we feel the α^2F function of Fig. 5 is probably fairly close to the actual α^2F of zinc.

The calculated α^2F functions in Figs. 5–7 are somewhat noisy due to the fact that we took a limited number of points in the Monte Carlo integration. By taking more points we can cut down on this noise. However, we have found on doing this for a few test cases that we still obtain the same results for $\lambda(\vec{k})$, $\Delta(\vec{k})$, and the transport properties. This is due to the fact that these properties are obtained by integrations over α^2F with smooth functions as weighting functions. For such integrals one gets nearly the same results if one first averages α^2F values over the nearest two or three bins to obtain the α^2F value in a given bin. Such an averaged function obtained from any of our α^2F functions given here is quite smooth, showing that we have taken enough random points in the Monte Carlo procedure. However, with the noise in these functions as presented here, it is not as easy to see the van Hove singularities that occur.

Figures 6 and 7 give anisotropic α^2F functions for \vec{k} in two particular directions on the Fermi surface in the extended-zone scheme. The calculations for these graphs used the same pseudopotential as in Fig. 5, namely, that of SF extrapolated to Appapillai and Williams at small \vec{q} . The band velocity in Eq. (23) was that of the non-local SF, but the final integral was multiplied by the factor (0.615/0.54) to correct for the modification of v_b due to the energy dependence of the pseudopotential.

Figure 6 is for \vec{k} in the c direction, which is at the center of the flat part of the lens. The corresponding α^2F has peaks at ω/ω_c equal to 0.30, 0.38, 0.50, and 0.88, which is at the same places as peaks in the isotropic α^2F , with all of these peaks much larger here than for the isotropic case. However, the peak at 0.65 does not appear in this direction, and there is an additional peak at 0.34.

Figure 7 is for \vec{k} at the edge of the lens in the $GKHA$ plane. The properties on the lens are nearly independent of the angle ϕ , and thus α^2F is very similar to Fig. 7 for any point on the edge of the lens. Again peaks occur for ω/ω_c equal to 0.30, 0.38, 0.50, and 0.88. Also, as in Fig. 6,

not only is the peak at 0.65 missing, but the entire region from 0.60 to 0.80 is quite small (note that the ordinate scale in Fig. 7 is different than in Figs. 5 and 6). On the other hand, the magnitude in the region around 0.3 is much larger for both of these points on the lens than is the average over the Fermi surface for this frequency region, i.e., in Fig. 5. This is an important factor in the anisotropy.

The most important part of the anisotropy in the α^2F functions is in the low-energy peaks at ω/ω_c equal to 0.30 and 0.38. It is these peaks that make the greatest contribution to the physical quantities of interest. These peaks are much larger for \vec{k} on the lens than for \vec{k} on the monster. We can understand this in terms of the $(\vec{k} - \vec{k}') \cdot \epsilon^\lambda(\vec{q}, m)$ factor in the electron-phonon matrix element of Eq. (20). The low energies that we are considering involve mostly phonons that are polarized parallel to the c axis. For \vec{k} vectors on the lens there are many \vec{k}' vectors such that $\vec{k} - \vec{k}'$ has a large component parallel to the c axis. For \vec{k} on the monster there are not the possibilities for forming $\vec{k} - \vec{k}'$ vectors with large components in the c direction. The low-energy phonons involved are transverse, which one tends to think do not interact well with the electrons. However, this is not true for umklapp processes, nor is it true for normal processes for \vec{q} not in a high-symmetry direction.

V. MASS ENHANCEMENT AND ENERGY GAP

In this section we give our results for the effective mass and the anisotropic energy gap based on our calculated α^2F functions.

The electron quasiparticle of wave vector \vec{k} has an energy ω relative to the Fermi energy, given by

$$\omega = |\epsilon_{\vec{k}} - \epsilon_F| + \Sigma(\vec{k}, \omega), \quad (26)$$

where $\epsilon_{\vec{k}}$ is the band-structure energy, as in Sec. III. $\Sigma(\vec{k}, \omega)$ is the self-energy and is a function of the quasiparticle energy. Σ is also a function of the direction of \vec{k} , but is relatively insensitive to the magnitude of \vec{k} for \vec{k} near the Fermi surface.⁴⁶ The energy ω in Eq. (26) is the location of the pole in the single-particle Green's function of the electron system.

By virtue of Migdal's theorem, the self-energy can be determined to all orders in the electron-phonon interaction and to order $(m/M)^{1/2}$.⁴⁶ Very close to the Fermi surface (excitation energies small compared to the Debye energy) and at low temperatures, the imaginary part of Σ vanishes and the real part has the form

$$\Sigma(\vec{k}, \omega) = -\lambda_{\vec{k}} \omega, \quad (27)$$

where $\lambda_{\vec{k}}$ depends only on the position on the Fermi surface and is independent of ω for small ω . $\lambda_{\vec{k}}$ is given by

$$\lambda_{\vec{k}} = 2 \int_0^{\infty} \frac{d\omega}{\omega} \alpha^2 F(\vec{k}, \omega). \quad (28)$$

The Fermi-surface average of $\lambda_{\vec{k}}$, denoted by λ , is by Eqs. (28) and (24)

$$\lambda = 2 \int_0^{\infty} \frac{d\omega}{\omega} \alpha^2 F(\omega). \quad (29)$$

λ is the quantity that, as pointed out by McMillan,³⁹ plays an important role in determining the superconducting transition temperature T_c .

Using Eq. (27) in Eq. (26) gives, for the quasiparticle energy,

$$\omega = |\epsilon_{\vec{k}} - \epsilon_F| / (1 + \lambda_{\vec{k}}), \quad (30)$$

so that the quasiparticle velocity is

$$\vec{v}_{\vec{k}} = \vec{\nabla}_{\vec{k}} \omega = \vec{v}_b / (1 + \lambda_{\vec{k}}), \quad (31)$$

where we have used Eq. (10) for the band velocity. Equation (31) can be interpreted as an increase in the effective mass by the factor $(1 + \lambda_{\vec{k}})$. This manifests itself in the cyclotron resonance frequency and, in terms of the Fermi-surface average λ , in the electronic specific heat.

The electron effective mass and hence the physical quasiparticle velocity are also affected by the electron-electron interaction. However, estimates of this indicate that it is much smaller than the mass enhancement due to the electron-phonon interaction. Also, the contribution from the electron-electron interaction would probably be much more isotropic than for the electron-phonon interaction.

Table III lists the values of the isotropic λ for zinc for various calculations. The first five columns are for various calculations we have made in this work. The first value of $\lambda = 0.334$ is for multi-OPW wave functions on the true Fermi surface using the SF pseudopotential extrapolated to Appapillai and Williams at small \vec{q} . That is, it is the λ calculated by Eq. (29) from the $\alpha^2 F$ of

Fig. 5. This value is about 12% too low compared with McMillan's λ of 0.38 (column 8) obtained from T_c , or 22% too low compared with the λ obtained from the experimental electronic specific heat assuming ρ_b is 0.61 (column 9). It should be pointed out that the λ from the specific heat is less accurate than that from T_c , since the former depends on the relatively uncertain value of ρ_b . Furthermore, it is $1 + \lambda$ rather than λ that is proportional to the specific heat.

The second column of Table III gives a λ of 0.36 for the multi-OPW wave functions on the true Fermi surface using the SF pseudopotential which extrapolates to SOMP at small \vec{q} . Columns 3, 4, and 5 are values obtained with the same pseudopotential as in column 2, but with one-OPW wave functions on the true Fermi surface, one-OPW wave functions on a spherical Fermi surface with the Fermi surface cut out in the directions in which the true Fermi surface does not exist, and one-OPW wave functions on the spherical Fermi surface with $\alpha^2 F$ multiplied by ρ_b , respectively.

The sixth and seventh columns of Table III are the results obtained by Truant and Carbotte¹⁴ and by Allen and Cohen.⁸ Both of these calculations were for one-OPW wave functions on a spherical Fermi surface with the result multiplied by $\rho_b = 0.59$ taken from Allen, Cohen, Falicov, and Kasowski.⁸ As we have discussed above, we believe that with the pure SF pseudopotential the value of ρ_b that is obtained is 0.54. The main difference between the Truant and Carbotte calculation and that of Allen and Cohen is that the former group used a much more realistic phonon model with the actual anisotropies, while the latter group used an isotropic phonon model.

Allen and Cohen concluded⁸ that "a reliable value of λ can be found provided the correct pseudopotential and phonon spectrum are known, even if effects of phonon anisotropy and departure from free-electron behavior of the conduction electrons are ignored." They concluded this on the basis of calculating λ for a number of simple metals, including zinc, in which they ignored

TABLE III. Isotropic λ of Eq. (29) for zinc obtained from various calculations.

Multi-OPW true Fermi- surface. SF to Appapillai and Williams	Multi-OPW true Fermi surface SF to SOMP	One-OPW true Fermi surface SF to SOMP	One-OPW cut-out FS SF to SOMP	One-OPW spherical FS SF to SOMP	Truant and Carbotte ^a	Allen and Cohen ^b	McMillan ^c from T_c	Specific heat with $\rho_b = 0.61$
0.334	0.36	0.39	0.38	0.41	0.425	0.42	0.38	0.43

^a Reference 14.

^b Reference 8.

^c Reference 39.

both the phonon anisotropy and the departure from free-electron behavior of the conduction electrons. They found values of λ that agreed to within 10%–50% of the λ obtained from the superconducting T_c . On the basis of our more extensive calculations for zinc, we agree with this conclusion if one considers 10%–50% error reliable. If one wants to use the λ to predict a T_c to 10%–50%, then the λ must be known much more accurately. We discuss this in more detail in Sec. VII.

We have calculated the anisotropic $\lambda_{\vec{k}}$ at a number of places on the Fermi surface using Eq. (28). Figures 8 and 9 give the results for four different models. In both of these figures the value of λ is given as a function of θ , the angle with c axis in the extended-zone scheme. Figure 8 is for $\phi = 0$, corresponding to the slice of the Fermi surface in Fig. 3(a), while Fig. 9 is for $\phi = \frac{1}{6}\pi$ corresponding to the Fermi surface in Fig. 3(b). Curve 1 as well as the individual points are for multi-OPW wave functions on the true Fermi surface, curve 2 is for single-OPW wave functions on the true Fermi surface, while curve 3 is for single-OPW wave functions on the spherical Fermi surface. The numbered curves were obtained using the SF pseudopotential extrapolated to SOMP at small q , while the individual points were calculated using the SF pseudopotential extrapolated to Appapillai and Williams at small q . Note that the anisotropy is very nearly the same for the multi-OPW wave functions on the true Fermi surface with either pseudopotential. However, the anisotropy is quite

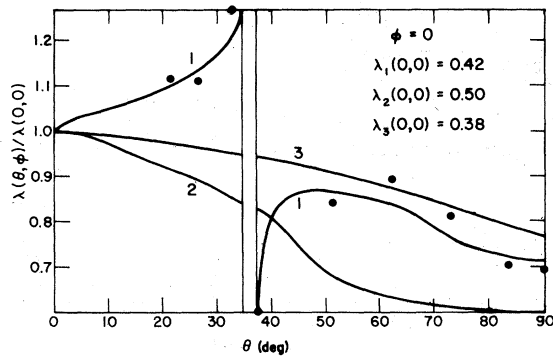


FIG. 8. Calculated anisotropic values of λ as a function of the angle θ with the c axis in a plane in the extended zone scheme that includes the $[11\bar{2}0]$ direction. Curve 1 is for multi-OPW's on the true Fermi surface, curve 2 is for one OPW on the true Fermi surface, and curve 3 is for one OPW on the spherical Fermi surface. These three calculations are for the SF pseudopotential extrapolated to SOMP for small wave vectors. The points are calculated using multi-OPW's on the true Fermi surface and with the SF pseudopotential extrapolated to Appapillai and Williams for small wave vectors.

different for either one-OPW wave functions on the true Fermi surface or for one-OPW wave functions on the free-electron sphere compared to the more realistic calculations.

Notice that there is a large discontinuity in λ for the multi-OPW case in going from the lens to the monster; i.e., in going across a Bragg plane in the extended zone scheme. This comes about for exactly the same reason that there is a discontinuity in the band energy on going across a Bragg plane—namely, it is due to the fact that the multi-OPW's have different relative phases on the two sides of the Bragg plane and hence certain quantities involved in matrix elements have different signs on the two sides. In the case of the band energy it is the matrix element of the potential energy between different plane waves in the expansion of the electron wave function that changes sign. In the case of λ , it is the sign of the matrix element of the electron-phonon interaction between certain of the plane waves in the wave function for \vec{k} and the wave function for \vec{k}' . Although it is the square of the matrix element between the electron wave functions that enters λ and thus there cannot be a negative overall contribution, with multi-OPW wave functions the contributions from the different plane waves are added before the result is squared. Thus there will be a discontinuity in the square of the matrix element as \vec{k} moves across a Bragg plane because of the relative phase changes of components of \vec{k} . See the Appendix for more details.

Our results for the anisotropic λ near the Bragg plane for the multi-OPW cases are quite different from what was predicted by Havinga.⁴⁷ He argued that with multi (or "mixed") OPW wave functions, "any intersection or close approximation of the Fermi surface by reasonable strongly scattering Bragg planes tends to increase $V \dots$," where V

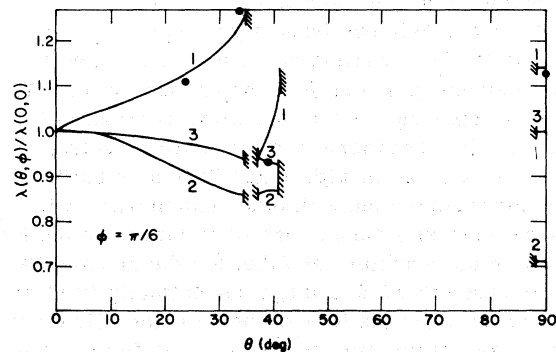


FIG. 9. Calculated anisotropic values of λ as a function of the angle θ with the c axis in a plane in the extended-zone scheme that includes the $[10\bar{1}0]$ direction. The notation is the same as in Fig. 8.

is the effective electron-electron interaction due to phonons that produces the superconducting state. Thus V is closely related to our isotropic λ and an increase in one follows from an increase in the other. Since the isotropic λ is a Fermi-surface average of the anisotropic $\lambda_{\vec{k}}$, Havinga's argument is that the anisotropic $\lambda_{\vec{k}}$ should be larger for \vec{k} near a scattering Bragg plane. We see that this is true at the rim of the lens; i.e., for θ equal to or slightly less than 34° in Figs. 8 and 9. However, just the opposite is true for \vec{k} on the inside rim of the monster at ϕ equal to zero; i.e., for θ equal to or slightly larger than 37° in Fig. 8.

In his analysis, Havinga does not consider the relative phase changes in the multi-OPW wave functions as \vec{k} crosses a Bragg plane. He also argues that the pseudopotential has its largest effect for small \vec{q} , but neglects the factor $\vec{q} \cdot \vec{\epsilon}^\lambda$ in the electron-phonon matrix element of Eq. (20). This factor causes the scattering to be zero at very small angles (small \vec{q}). For umklapp processes in which $(\vec{G} + \vec{q}) \cdot \vec{\epsilon}^\lambda$ is not small for small \vec{q} , the interaction still goes to zero as \vec{q} goes to zero, as discussed by Sham and Ziman.⁴⁸

Another author who has considered the anisotropic λ in zinc is Auluck.²⁴ As we have discussed in the Introduction, Auluck determines the anisotropic $\lambda_{\vec{k}}$ [or the mass-enhancement factor $(1 + \lambda_{\vec{k}})$] by comparing the calculated band mass of Stark and Auluck²⁵ with the cyclotron resonance mass of Sabo⁴⁹ on various cyclotron orbits. However, Stark and Auluck derived their nonlocal pseudopotential on the *assumption* that the anisotropic $\lambda_{\vec{k}}$ on the lens is constant. We see from our calculations of $\lambda_{\vec{k}}$, Figs. 8 and 9, that this function is far from being constant. However, we agree with the conclusion of Stark and Auluck that the SF band mass and band velocity must be modified. They argue that this modification is necessary because of the effect of the filled d bands near the Fermi surface on the pseudopotential of zinc.

We previously published a graph of the anisotropic $\lambda_{\vec{k}}$ as a function of θ for $\phi = 0$ for zinc,¹ corresponding to Fig. 8 of the present paper. The result reported there is much the same as in Fig. 8, namely, that there is much more anisotropy for the calculation with multi-OPW's on the true Fermi surface than with other calculations with more approximations, that $\lambda_{\vec{k}}$ is larger on the lens than on the monster, and that for the multi-OPW calculation there is a large discontinuity in $\lambda_{\vec{k}}$ at the break from the lens to the monster. However, there are some differences; e.g., $\lambda_{\vec{k}}$ in the previous calculation did not increase as much with θ on the lens for the multi-OPW case as in Fig. 8. The reason for the differences is that different phonon models were used in the two sets of calcu-

lations. The phonon model in the present calculation is superior to that in the previous calculation.

The electron-phonon mass enhancement also shows up in measurements of the electron quasiparticle Fermi velocity. This velocity has been measured on the lens in zinc by two types of measurements.^{50,51} Rahn and Sabo⁵⁰ used magnetic-surface-state measurements to determine the quasiparticle velocity as a function of position on the lens. We have reproduced their data in Fig. 10. $v_{\text{free}} = 1.837 \times 10^8$ cm/sec and is the free-electron Fermi velocity. The curves in Fig. 10 are the results of two of our calculations, in both cases using Eq. (31). The band velocity used was that of the solid curve in Fig. 4 for both curves in Fig. 10. For the solid curve in Fig. 10, λ_1 of Fig. 8 (multi-OPW wave functions on the true Fermi surface) was used for the renormalization, while for the dashed curve λ_3 of Fig. 8 (one-OPW wave functions on the spherical Fermi surface) was used for the renormalization.

Notice that our more realistic calculation gives a better fit to the data, not only in terms of the total magnitude (Rahn and Sabo claim an overall probable error of about 4%, so the difference between our dashed curve and their data may not be significant), but also in terms of the shape of the curve. There is an increase in the band velocity on moving from the center of the lens out to about 0.9 of the distance to the rim. We believe it is this increase in the band velocity that causes the

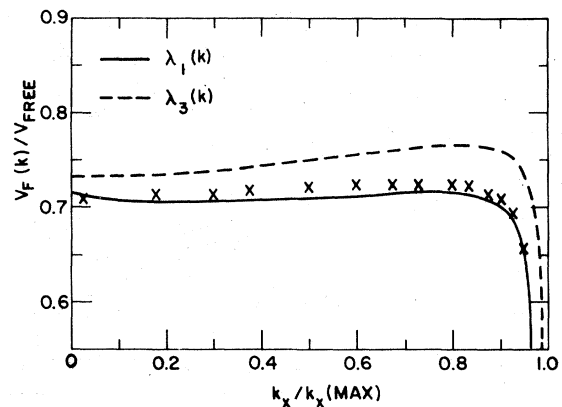


FIG. 10. Electron quasiparticle Fermi velocity normalized to the free-electron value v_{free} as a function of position on the lens. $k_x(\text{max})$ is the radius of the lens. The curves are our calculated results using Eq. (31). The solid curve is with the renormalization of the velocity by $\lambda_1(\vec{k})$ of Fig. 8 (multi-OPW wave functions on the true Fermi surface), while the dashed curve is with the renormalization by $\lambda_3(\vec{k})$ of Fig. 8 (single-OPW wave functions on the spherical Fermi surface). The band velocities for both curves were taken from the solid curve of Fig. 4. The crosses are experimental points from Rahn and Sabo (Ref. 50).

initial increase in quasiparticle velocity that Rahn and Sabo detected. We believe that they are incorrect in attributing this to the variation in the renormalization. They state that they have an inaccuracy due to statistical fluctuations in locating the peak positions of less than 1%; so presumably this 3% change in velocity is real. The dashed curve in Fig. 10 is the resultant variation in quasiparticle velocity when there is practically no variation in the renormalization (curve 3 in Fig. 8). In fact, what we think is the true variation in the renormalization (curve 1 in Fig. 8) tends to cancel the variation in the band velocity so that the quasiparticle velocity is rather flat out to near the rim. Very near the rim the rapidly increasing $\lambda_{\vec{k}}$ (curve 1 of Fig. 8) and the rapidly decreasing v_b (the solid curve of Fig. 4) combine to cause the rapid decrease of the quasiparticle velocity. Even if the dashed curve is shifted down in Fig. 10, the fit cannot be made as good with the experimental data as in the case of the realistic calculation (the solid curve) with no fitting.

Rowell has also measured the electron quasiparticle energy in the c direction in zinc.⁵¹ He used the Tomasch effect (geometrical resonance) in a tunneling junction, and in the later of the two papers reports four quasiparticle velocities of 1.02×10^8 , 0.76×10^8 , 0.51×10^8 , and 0.44×10^8 cm/sec. None of these are near our calculated and Rahn and Sabo's measured velocity at the center of the lens of $v = 0.71 v_{\text{free}} = 1.30 \times 10^8$ cm/sec. However, it has been suggested by Colucci, Tomasch, and Lee⁵² that, based on the theory of Wolf-

ram,⁵³ Rowell's results should be multiplied by 2. If this is done, his value of 0.76×10^8 cm/sec becomes 1.52×10^8 cm/sec, which is within 15% of our value. The other velocities may come from the monster, but we have not carried out detailed calculations to make a comparison there.

The superconducting properties including T_c , the anisotropic energy gap, and the temperature dependence of the gap, the specific heat, and the critical field can be calculated³ from the $\alpha^2 F$ functions by means of the Eliashberg equations.⁴⁶ We shall not be concerned with the temperature dependence of the superconducting properties in this paper, and we shall defer our discussion of T_c to Sec. VII. Here we present our results for the anisotropic energy gap.

The anisotropic energy-gap function at $T = 0$ satisfies the coupled Eliashberg nonlinear integral equations,⁴⁶ which involve the anisotropic gap under the integral. This set of integral equations could be solved by an iteration scheme in which the isotropic gap is substituted for the gap in the integral and a first approximation to the anisotropic gap is obtained. This first approximation is then substituted in the integral to obtain a second approximation, and so forth. This procedure was first done stopping at the first iteration by Bennett³⁸ and followed by others.^{9,10,54} Leavens and Carbotte¹⁰ showed, by carrying out a second iteration for the case of Al, that the gap anisotropy remained much the same as for the first iteration.

The first-order anisotropic gap function then is obtained from⁴⁶

$$\Delta(\vec{k}, \omega) Z(\vec{k}, \omega) = \int_0^{\omega_m} d\omega' \operatorname{Re} \left(\frac{\Delta(\omega')}{\sqrt{\omega'^2 - [\Delta(\omega')]^2}} \right) \left[\int_0^{\infty} d\Omega \alpha^2 F(\vec{k}, \Omega) \left(\frac{1}{\Omega + \omega' + \omega - i\delta} + \frac{1}{\Omega + \omega' - \omega - i\delta} \right) - \mu^* \right], \quad (32a)$$

and

$$[1 - Z(\vec{k}, \omega)] \omega = \int_0^{\omega_m} d\omega' \operatorname{Re} \left(\frac{\omega'}{\sqrt{\omega'^2 - [\Delta(\omega')]^2}} \right) \left[\int_0^{\infty} d\Omega \alpha^2 F(\vec{k}, \Omega) \left(\frac{1}{\Omega + \omega' + \omega - i\delta} - \frac{1}{\Omega + \omega' - \omega - i\delta} \right) \right]. \quad (32b)$$

In order to calculate the right-hand sides of Eqs. (32), we need to know the isotropic gap function $\Delta(\omega)$ and the Coulomb pseudopotential μ^* as well as the anisotropic $\alpha^2 F$ function. The value obtained from the right-hand side of (32a) is independent of the value of the cutoff of the integrals ω_m as long as ω_m is sufficiently large, and providing that μ^* is adjusted to the cutoff.⁶ We used $\omega_m = 10\omega_c$, where $\omega_c = 4.178 \times 10^{13}$ rad/sec is the maximum phonon frequency.

The isotropic gap function was first obtained by solving the isotropic Eliashberg equations [similar to Eqs. (32), but with the isotropic $\alpha^2 F$ on the right-hand side in place of the anisotropic $\alpha^2 F$]. We used the isotropic $\alpha^2 F$ obtained from the SF

pseudopotential extrapolated to SOMP at small values of Q . This function is very similar but not identical to that of Fig. 5. The Coulomb pseudopotential μ^* was adjusted so that the energy gap $\Delta_0 = \Delta(\Delta_0)$ took on the experimental value⁵⁵ of $\Delta_0 = 0.117$ MeV. The required value of μ^* was found to be 0.075, lower than the value suggested by McMillan³⁹ of $\mu^* = 0.12$, but in agreement with $\mu^* = 0.08$ given in Ref. 56.

Using these results together with the anisotropic $\alpha^2 F$ functions obtained from the multi-OPW wave functions on the true Fermi surface and the SF pseudopotential extrapolated to SOMP at small \vec{q} -values, we have obtained the anisotropic energy gap $\Delta_0(\vec{k}) = \Delta(\vec{k}, \Delta_0(\vec{k}))$ at a number of positions on

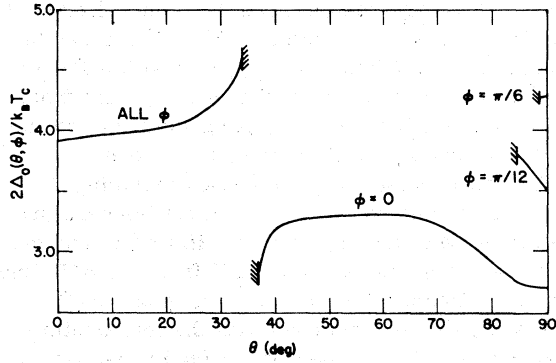


FIG. 11. Calculated anisotropic superconducting energy gap $2\Delta_0(\vec{k})$ at $T = 0$ normalized by $k_B T_c$ as a function of position on the Fermi surface. The results were obtained using Eqs. (32) with the anisotropic $\alpha^2 F(\vec{k}, \omega)$ obtained using multi-OPW wave functions on the true Fermi surface and with the SF pseudopotential extrapolated to SOMP at small \vec{q} .

the Fermi surface. In Fig. 11 we have plotted this function in terms of $2\Delta_0/k_B T_c$ (this quantity takes the value 3.53 for the weak-coupling isotropic BCS superconductor) as a function of θ for three values of ϕ on the Fermi surface in the extended zone scheme.

We find with our multi-OPW true Fermi-surface model, as did Truant and Carbotte⁵⁴ for the one-OPW spherical Fermi-surface model of zinc, that the anisotropic gap varies over the Fermi surface in much the same way as the anisotropic $\lambda_{\vec{k}}$. This can be seen by comparing Fig. 11 with curves 1 in Figs. 8 and 9. Also, as with the case of the anisotropic $\lambda_{\vec{k}}$, the anisotropic gap is quite different for our model with the realistic electrons than with the one-OPW electrons on the spherical Fermi surface, particularly near Bragg planes.

One of the ways the anisotropy in the energy gap shows up experimentally is in the anisotropy of the ultrasonic attenuation in a single crystal. Such measurements have recently been reported on zinc by Cleavelin and Marshall⁵⁷ and by Dobbs, Lea, and Peck.⁵⁸ For sound propagating in a

TABLE IV. Comparison of the calculated anisotropic energy gap averaged over the effective zone with the experimental results from ultrasonic attenuation.

Propagation direction	Effective zone	Calculated	$2\langle\Delta(\vec{k})\rangle/k_B T_c$	
			Experimental	
[11 $\bar{2}$ 0]	$\phi = 30^\circ$	4.14	3.80 ^a	3.64 ^b
[10 $\bar{1}$ 0]	$\phi = 0^\circ$	3.27	2.82 ^a	3.79 ^b
[0001]	$\theta = 90^\circ$	3.50	3.02 ^a	3.41 ^b

^a Cleavelin and Marshall (Ref. 57).

^b Dobbs, Lea, and Peck (Ref. 58).

given direction, the attenuation is a function of the average of the gap in an extremal belt on the Fermi surface perpendicular to the propagation direction. In Table IV we compare the results of crudely averaging our anisotropic gap over this belt or effective zone with the experimental results^{57,58} for each of three directions of propagation. Although there is not quantitative agreement between our calculation and either set of experimental data, neither is there agreement between the two sets of experiments. However, it is probably better to compare the ratios of the gaps for different zones, since the absolute value of our anisotropic gap is obtained from only one iteration of the gap equation using the isotropic gap as the trial function. Leavens and Carbotte¹⁰ showed that the first iteration gives the correct anisotropy but not the correct absolute magnitude of the gap.

Table V gives the ratio of the gaps in a particular zone to those in the zone corresponding to propagation in the [0001] direction. Such ratios give an indication of the degree of anisotropy of the gap. We see that our calculated ratios agree rather well with the measurements of Cleavelin and Marshall,⁵⁷ but they do not agree at all with the measurements of Dobbs, Lea, and Peck.⁵⁸

The measurements of Dobbs, Lea, and Peck indicate that there is very little variation in the average gap between the three zones. This is not inconsistent with a large anisotropy in the gap as a function of position on the Fermi surface, since the averaging over the zone could sample the gaps in such a way that in each of the three zones considered the average is the same. However, this seems unlikely. Thus the measurements of Dobbs *et al.*⁵⁸ appear to be inconsistent with other types of measurements which do show an anisotropy in the gap of 15% or so.⁵⁹⁻⁶¹ For example, Duclaux and Cheeke⁵⁹ found this large variation of the energy gap when they analyzed their specific-heat data on superconducting Zn. Zavaritskii⁶⁰ measured anisotropy in the thermal conductivity in superconducting zinc, which indicates that the maximum energy gap $2\Delta_{\max}$ is in the c direction and is about $3.6 k_B T_c$, while the minimum gap $2\Delta_{\min}$ occurs in the plane and is about $2.4 k_B T_c$. Although

TABLE V. Ratios of anisotropic energy gaps of Table IV for two different directions.

Directions	Ratios of $\langle\Delta(\vec{k})\rangle$	
	calculated	Experimental
[11 $\bar{2}$ 0], [0001]	1.18	1.26 ^a 1.07 ^b
[10 $\bar{1}$ 0], [0001]	0.93	0.93 ^a 1.11 ^b

^a Cleavelin and Marshall (Ref. 57).

^b Dobbs, Lea, and Peck (Ref. 58).

his analysis was based on an ellipsoidal model of the gap anisotropy and thus does not correspond to the real anisotropy, it still should give us some indication of the anisotropy. We see that the deviation of the maximum and the minimum from some average is about 20% in Zavaritskii's results. This is consistent with our calculated results. We do not find the maximum gap in the c direction but the maximum is on the lens (see Fig. 11), and the average on the lens is larger than the average on the monster. The former average is roughly $4.3 k_B T_c$. Thus we find about the same anisotropy as does Zavaritskii, and our maximum is roughly in the same direction as his.

Microwave-absorption measurements on single crystals of superconducting zinc⁶¹ also give an anisotropy of the energy gap. Hays' analysis of this data indicates that there is a gap on the lens of $4.0 k_B T_c - 4.9 k_B T_c$, while the average over the rest of the Fermi surface is approximately $3.1 k_B T_c$. Hays states that the gaps he finds are consistent with the data of Dobbs *et al.*⁵⁸ However, Hays is taking a gap that already has a certain amount of averaging over the Fermi surface, and he does further averaging to obtain his model values for the ultrasonic attenuation. Thus we think that the data of Evans, Garfunkel, and Hays⁶¹ shows more anisotropy of the energy gap than does the data of Dobbs *et al.*⁵⁸

VI. CYCLOTRON RESONANCE

Another experiment in which the electron-phonon interaction shows up in the electronic properties is in Azbel'-Kaner cyclotron resonance. Whereas magnetic-surface-state measurements determine the values of λ_k^* point by point on the Fermi surface, cyclotron resonance gives λ_k^* averaged over a line around the Fermi surface, the cyclotron orbit.

Although large anisotropies are measured in the cyclotron mass,^{49,62} only a very small part is due to anisotropies in λ_k^* . Two other sources of the anisotropy are the breaking up of the Fermi sphere by Bragg planes and the anisotropy of the band mass as reflected in the anisotropy in the band velocity. Since the geometrical shape of the Fermi surface is well established, we have divided the cyclotron mass m_c by $(\hbar/2\pi)\oint d\vec{k}/v_{F\perp}$, where the integral is around the cyclotron orbit on the true Fermi surface and $\vec{v}_F = \hbar\vec{k}_F/m$ is the free-electron velocity. $v_{F\perp}$ is the component of \vec{v}_F that is perpendicular to the magnetic field. By dividing by this factor we have normalized out the anisotropy due to the breaking up of the Fermi surface by Bragg planes and due to other geometrical factors. That is, with electrons with a band

velocity equal to the free-electron band velocity (band mass equal to the free-electron mass m) and with λ_k^* equal to zero, the normalized cyclotron mass m_c would then have the value m regardless of the shape of the Fermi surface and regardless of the particular orbit chosen.

In Figs. 12-15 are plotted the ratio of the cyclotron mass to the free mass m_c/m normalized by the factor given above. We see that much of the anisotropy of the measured cyclotron mass has disappeared on using the normalization factor. This is especially true for the lens central orbit masses in Fig. 12, where in the experimental data the mass varies by over a factor of 2. The anisotropy that remains in Figs. 12-15 is due entirely to anisotropies in the band mass and in λ_k^* .

The experimental curves in Figs. 12-15 are given by the dashed lines with the triangles for Sabo's results⁴⁹ and the solid dots for Brookbanks' results.⁶² The triangles and dots are not experimental points, but are points calculated by us using points from their experimental curves of the cyclotron mass. The error bars indicate the estimated accuracy to which we could read the experimental graphs. The experimental errors were less than these error bars, according to both Brookbanks and Sabo.

The results from three of our calculations are

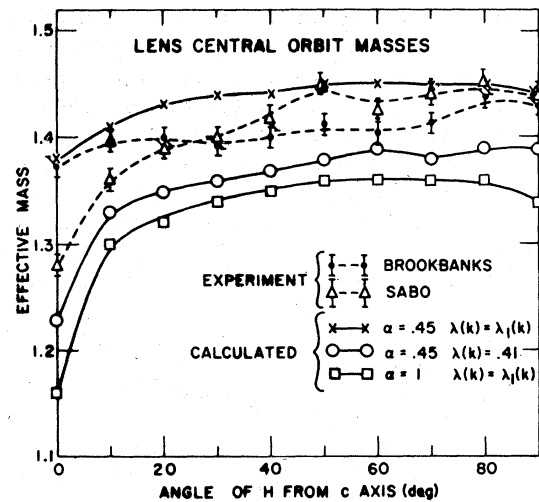


FIG. 12. Normalized or effective cyclotron mass for the central orbits on the lens as a function of the angle θ of the magnetic field with the c axis. Our calculated results are from Eq. (33), with the band velocities from Eq. (18) for two different values of α . The \times 's and squares are with the anisotropic λ_k^* , while the open circles are with a constant λ_k^* . The calculated points are joined by solid lines. The solid circles and the triangles joined by the dashed curves are our normalization of the experimental cyclotron masses of Brookbanks (Ref. 62) and Sabo (Ref. 49). See text for an explanation.

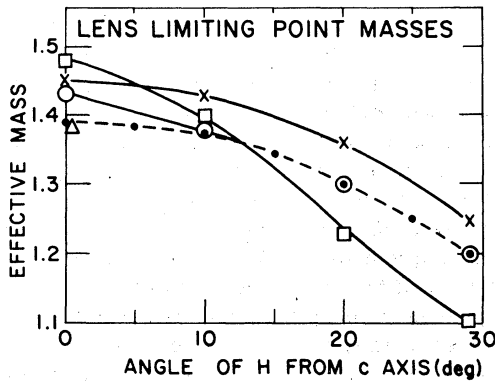


FIG. 13. Effective cyclotron mass for the limiting point orbits on the lens as a function of the angle of the magnetic field with the c axis. Solid lines connect calculated points, while the dashed line connects our normalization of experimental points. The notation is the same as in Fig. 12

also given in Figs. 12–15 in each case obtained with the effective mass m_{eff} from

$$m_{\text{eff}} = \frac{\oint d\vec{k}(1 + \lambda_k)/[v_b(k)]_x}{\oint d\vec{k}/v_{F\perp}}, \quad (33)$$

where the integrals in both the numerator and denominator are around the cyclotron orbit on the true Fermi surface. The best calculation, denoted by the x 's, is with λ_k^+ from curve 1 of Figs. 8 and 9 and with the band velocity v_b from Eq. (18) with $\alpha = 0.45$ (the solid curve of Fig. 4 for the lens) substituted in Eq. (33). The open circles are with the same band velocity, but with λ_k^+ taken as a constant equal to 0.41. The open squares give the calculated points with the realistic λ_k^+ of Figs. 8 and 9, but with v_b of Eq. (18) with $\alpha = 1.0$, i.e., with the unmodified SF band velocity. The solid lines are lines drawn through the calculated points.

We see in Figs. 12–15 that in each case the cal-

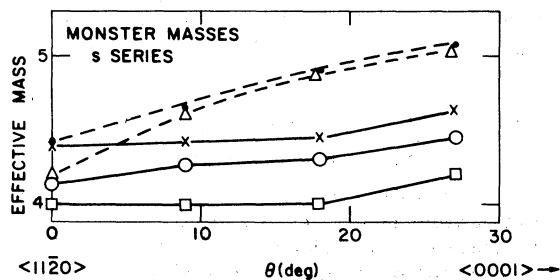


FIG. 14. Effective cyclotron mass for the s series on the monster as a function of the direction of the magnetic field in the $\Gamma K H A$ plane. Solid lines connect calculated points, while the dashed lines connect our normalization of experimental results. The notation is the same as in Fig. 12.

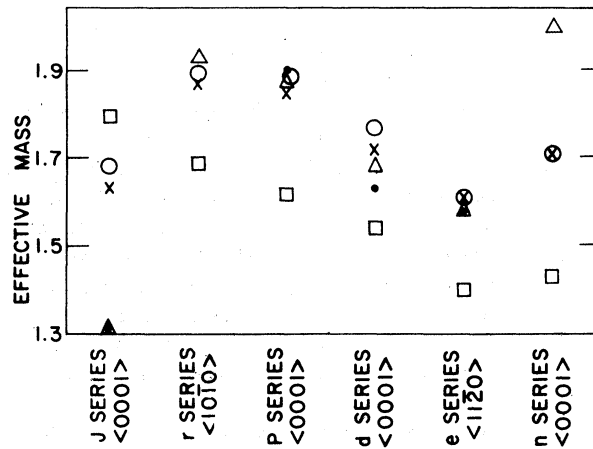


FIG. 15. Effective cyclotron mass for several orbits on the monster and needle. The x 's, open circles, and squares are our calculated results, while the closed circles and triangles are our normalization of experimental data. The notation is the same as in Fig. 12.

culated results with the unmodified SF band velocity does not fit the experimental data nearly as well as the results with the nonlocal contribution to the band velocity decreased, either with the anisotropic λ_k^+ or with a constant λ_k^+ . This is further evidence which, together with the arguments given in Sec. III, leads us to believe that the band velocity obtained from the unmodified SF nonlocal pseudopotential is not correct for zinc.

Except for the central orbit on the lens, the two calculations with the modified SF band velocity (the x 's and the open circles in Figs. 12–15) give very nearly the same results. That is, except for the lens central orbit, one can scarcely see the effect of the anisotropy of λ_k^+ . The reason is that although λ_k^+ appears to be very anisotropic in curve 1 of Figs. 8 and 9, the variation is only about 20% about the mean. In the cyclotron mass it is $1 + \lambda_k^+$ which occurs, and with $\lambda \sim 0.4$, the variation of $1 + \lambda_k^+$ is only approximately 6% about the mean. Further the cyclotron mass does not represent a point value on the Fermi surface but is an average over a cyclotron orbit. This further washes out the anisotropy in the cyclotron mass due to anisotropy in λ_k^+ .

For the central orbit masses on the lens there are differences between the result with an isotropic λ and that with the anisotropic λ_k^+ that are large enough to show up experimentally. First we see that with the constant $\lambda = 0.41$, which is the value that gives good agreement with the limiting point masses on the lens (Fig. 13), and with the different orbits on the monster (Figs. 14 and 15), the effective mass is too small compared with the experiments for the central orbit mass on the lens.

Thus the experiments show that $\lambda_{\vec{k}}$ on the lens particularly near the rim must be larger on the average than on the monster. The limiting point orbits are on the center of the flat part of the lens, so the larger $\lambda_{\vec{k}}$ near the rim of the lens does not contribute to these orbits. However, the $\lambda_{\vec{k}}$ near the rim of the lens contributes to all of the lens central orbits, particularly those in which the magnetic field is along or near the c axis. Our conclusion on this point is similar to that of Auluck,²⁴ who also found that the experimental data requires that $\lambda_{\vec{k}}$ on the lens be larger than on the monster. See his Table III.

It is precisely for the central orbits on the lens, where there is the greatest difference between the calculation with a constant $\lambda_{\vec{k}}$ and that with the anisotropic $\lambda_{\vec{k}}$, that there is the greatest difference between the data of Brookbanks⁶² and of Sabo.⁴⁹ Although our curves based on the experimental data of Brookbanks and of Sabo in Fig. 12 differ somewhat over the entire θ range, where θ is the angle of H with the c axis, Brookbanks states that his results are in good agreement with Sabo for these orbits except for an interval of 15° about the $\langle 0001 \rangle$ direction. We see that our derived curves from the experimental curves are nearly within our estimated errors of each other for θ greater than 15° . However, for θ smaller than 15° the two curves based on the experiments are quite different.

Brookbanks' effective mass is nearly independent of angle, the kind of dependence one would get from an isotropic band mass and an isotropic $\lambda_{\vec{k}}$. In fact, Brookbanks states in his paper⁶² that "When the anisotropy of m^* for branch a (the lens central orbit) was compared with the nearly-free-electron prediction, it was found that the enhancement factor was very nearly constant over the whole angular range, falling slightly in the region of the c axis." We see in Fig. 12 that this is exactly what we would conclude from his data if the band mass were a constant. However, the band mass is not a constant on the lens. And if we take a band mass based on the modified or even the unmodified SF pseudopotential (only the former is plotted in Fig. 12), a constant $\lambda_{\vec{k}}$ leads to an effective mass that drops rather sharply for the magnetic field near the c axis. This is given by the curve with the open circles in Fig. 12. If we consider our calculated $\lambda_{\vec{k}}$, which increases rather strongly near the rim of the lens, this increase in $\lambda_{\vec{k}}$ tends to compensate for the decrease in the band mass, and the resulting curve (the \times 's in Fig. 12) decreases only slightly as the magnetic field approaches the c axis. Remember that as the field approaches the c axis, the central cyclotron orbit samples more and more of the

rim of the lens. Brookbanks' data is in agreement with our best calculation, in which the anisotropy of the band mass is nearly canceled by the anisotropy of $\lambda_{\vec{k}}$. And, in fact, we interpret the slight decrease in the mass as the field approaches the c axis not as a decrease in the enhancement factor but as a decrease in the band mass, which is not quite compensated by the *increase* in the enhancement factor. Brookbanks was quite aware that a compensation must be taking place between these two anisotropies and he states so in his paper.

On the other hand, Sabo's results for the effective mass in Fig. 12 show a relatively small variation with θ for $\theta > 20^\circ$ but a 10% drop between $\theta = 20^\circ$ and $\theta = 0^\circ$. This is the same type of variation that we find with the modified SF pseudopotential and a constant $\lambda_{\vec{k}}$. Auluck²⁴ also concluded, on comparing the Stark and Auluck band mass²⁵ (which seems to be similar to our modified SF band mass) with the data of Sabo, that $\lambda_{\vec{k}}$ is constant on the lens. However, the Stark and Auluck pseudopotential was derived on the assumption that the mass renormalization is a constant on the lens. We do not think that this assumption is justified.

Inasmuch as the experiments disagree on this important measurement, we can not say that cyclotron resonance shows whether or not there is an anisotropy in $\lambda_{\vec{k}}$. However, the one experiment (Brookbanks) does agree quite well with our best calculation. And this calculation is based on the same model that gives results in good agreement with the Fermi-surface velocity measurements of Rahn and Sabo⁵⁰ and the ultrasonic-attenuation measurements in the superconductor by Cleavelin and Marshall.⁵⁷ Because the difference between Sabo and Brookbanks involves the question of whether or not there is a sharp change for H lined up with the c axis compared to H being 10° or so away from the c axis, there is always the question of whether or not H really was well aligned in the experiment. It appears from Fig. 12 that Sabo has observed the sharp change and Brookbanks has not, so one might question whether Brookbanks might have missed the alignment; in fact, in the experimental cyclotron mass it is really Brookbanks who has observed the sharp change in mass near $\theta = 0$ and Sabo has not. It is the sharp change in orbit path length that we have used, combined with Sabo's relatively small change in cyclotron mass for small θ , that have combined to give the large change in effective mass in Fig. 12. In Brookbanks' case the large change in orbit path tended to cancel his observed large change in cyclotron mass to give the small change of his effective mass in Fig. 12.

At this point we can compare the average $\lambda_{\vec{k}}$

which fits the cyclotron resonance data with the λ that fits the specific-heat data. We have seen that if we assume $\lambda=0.41$ we obtain reasonable agreement with all of the cyclotron orbits, with the possible exception of $\theta < 15^\circ$ on the lens central orbits. On the other hand, we have seen in Table III that $\lambda=0.43$ from the specific-heat data. Thus these two experimentally determined values of λ are in reasonable agreement with each other and with the $\lambda=0.38$ obtained from T_c . Of course, the cyclotron resonance determination of λ as well as the specific-heat determination both depend on the band mass or band density of states that we use. However, we have used the same band density of states in both of our determinations of λ , and uncertainties in this band density of states would tend to cancel. That is, these determinations of λ may be off by 10% or 20% from the true λ , but one would hope that they would agree with each other to something better than this. In contrast, Auluck²⁴ found that λ obtained from cyclotron resonance data is 25%–30% higher than λ obtained from the specific-heat data, whether he used the unmodified SF pseudopotential or the Stark and Auluck pseudopotential (see his Table II). We do not understand these large differences that he obtained.

In Fig. 13 we have not put error bars on the effective masses obtained from Brookbanks' data on the limiting point orbits, because we obtained the experimental data from a graph of the b resonances in Brookbanks' thesis. We could read these data points to better than $\pm 2\%$, the latter being the experimental accuracy for these orbits. We have plotted only the one point from Sabo at $\theta=0^\circ$ but his measurements at larger θ are within 2% of Brookbanks' curve.

In Fig. 14 we have plotted the effective mass for the s series of orbits. These orbits are around the small horizontal arms of the monster. In order to do a reasonable calculation, it was necessary to increase the number of OPW's from five to ten. The reason is that both the circumference and the band mass of this orbit are extremely sensitive to the number of OPW's. Calculations with the true Fermi surface but a free band mass give results that are much too low, but when one considers the single OPW Fermi surface and free-electron-band mass the results are much better.

In Fig. 15 we have plotted single points from other cyclotron orbits. The j point was calculated assuming the orbit is on the inside rim of the monster, as suggested by Sabo. Brookbanks pointed out that this is not consistent with the known Fermi surface, but he could offer no other orbit for these observations. If it is correct that this is the inside rim of the monster, then the experi-

mental data suggest that λ_r decreases even more on going from the rim of the lens to the rim of the monster than we show in the discontinuity of λ_k in curve 1 of Fig. 8.

The r resonance and the n resonance were seen by Sabo but not by Brookbanks. For the calculation we used Sabo's interpretation of the former being the "dog bone" on the monster and the latter being on the needle. Our calculation on the needle is not as accurate as for other orbits.

The p , d , and e resonances were taken as suggested by both Sabo and Brookbanks to be the μ , γ , and σ orbits on the monster. See their papers for drawing of these orbits.

VII. CONCLUSIONS

We have carried out detailed calculations of electron-phonon effects in zinc using realistic models for the phonons, for the electrons, and for the electron-phonon interaction. Of much interest is whether calculations such as this can predict the superconducting transition temperature T_c . It is our view that if the normal-state properties were known to sufficient accuracy, then T_c could be determined with great accuracy. However, the normal-state properties are not known to arbitrary accuracy.

For such a prediction in T_c the Coulomb interaction μ^* between electrons must be known.³⁹ Here we follow McMillan's notation, in which the star on μ denotes the renormalized Coulomb interaction. Calculations such as those in this paper tell us nothing about the value of μ^* . Crude calculations of μ^* , together with estimates from anomalous tunneling and from the isotope effect, indicate that μ^* does not vary much from metal to metal and that for Zn it has the value of approximately 0.11 ± 0.01 .³⁰ A 10% error in μ^* is not so important for a strong-coupling superconductor such as Pb or Hg. Thus, for example, for a strong-coupling superconductor with $\lambda=1$ and $\mu^*=0.1$, a 10% error in μ^* leads to only a 2% error in the exponent in McMillan's formula and to only a 5% error in T_c . However, for Zn with $\lambda=0.38$ and $\mu^*=0.1$, a 10% error in μ^* leads to a 27% error in T_c . We could get more accurate results for T_c and the effect of errors in μ^* by a direct solution of the Eliashberg equations. However, McMillan's formula does give us better than an order of magnitude in the expected error in T_c with a given error in μ^* and/or in λ (see Allen or Dynes⁶³). The reason for the much larger effect in Zn is that for this superconductor the Coulomb repulsion nearly cancels the electron-phonon interaction, while in strong-coupling superconductors the electron-phonon interaction is quite a bit larger than the Coulomb

TABLE VI. Estimated errors in calculating T_c of zinc from errors in various normal-state electronic properties.

Normal-state electronic property	Origin of the error	Estimated error in the property	Resulting error in T_c
μ^*		$\pm 10\%$	$\pm 27\%$
λ	Spherical Fermi surface	$+90\%$	$+1393\%$
λ	Spherical Fermi surface corrected for actual area	$+14\%$	$+122\%$
λ	Band velocity-energy dependence of pseudopotential	$+14\%$	$+122\%$
λ	Extrapolation of pseudopotential to small q values	-30%	-97%

interaction. Thus small changes in μ^* have a much greater effect on T_c of weak-coupling superconductors such as Zn. Table VI summarizes the estimated errors in calculating T_c for zinc.

Errors in λ also produce enhanced errors in T_c . For example, if the true Fermi surface and multi-OPW wave functions are replaced by the free-electron Fermi sphere and one-OPW wave functions, our calculated λ increases by a factor of 1.90, leading to an increase in the superconducting T_c by more than a factor of 10, as given in the second line of Table VI.

If we correct this free-electron result by multiplying the free-electron λ by ρ_b , as was done by Allen *et al.*⁸ and by Truant and Carbotte,¹⁴ so that the large cut-out region of the Fermi surface and the non-free-electron-band velocities are corrected for at least approximately, we find a λ that is still 14% larger than our best result. Such an increase in λ for Zn leads to an increase in T_c by more than a factor of 2. This error is given on line 3 of Table VI.

Furthermore, if the SF band velocity is taken in the calculation of λ , one obtains an error in λ of $+14\%$ compared to the calculation using what we feel is a more reasonable band velocity (line 4 of Table VI). Finally, there is an error in λ of about -30% if one uses a straightforward extrapolation of the SF pseudopotential to small q values for calculating the electron-phonon matrix elements in determining λ , compared to using SOMP⁴³ or Appapillai and Williams⁴⁴ for the pseudopotential at small q (see the last line of Table VI).

We do not think that the prescriptions which we have used for the band velocity or the electron-

phonon matrix elements are orders of magnitude better than that from the straightforward use of SF. However, we feel that our arguments do show that the uncertainties in these quantities make a calculation of T_c for zinc to an accuracy of better than $\pm 100\%$ impossible. In the calculation of Ref. 8 the errors that we believe occurred there tend to cancel (the last three lines of Table VI), and thus those authors obtained a reasonable result for T_c . However, we think that this agreement was fortuitous.

We conclude that to obtain a reasonable value for T_c it is essential that a realistic treatment of the electrons and of the electron-phonon interaction be made. It is equally important to have a good model for the phonons. We have not investigated the effect of different phonon models on T_c . However, as we have discussed, the low-lying peaks in the phonon density of states determine the low-lying peaks in α^2F , which, in turn, have a critical effect on λ and on T_c .

For the anisotropic electron-phonon effects it is equally important that the theoretical model include all elements in a realistic manner. For example, the calculated $\lambda_{\mathbf{k}}$ and $\Delta_{\mathbf{k}}$ both have large discontinuities across Bragg planes when the electron wave functions are treated as an expansion of several OPW's. These discontinuities do not occur in calculations with single OPW wave functions whether on a spherical Fermi surface or on the true Fermi surface.

Of the different parts of the total model, the lattice dynamics^{23,31} and the geometry of the Fermi surface^{21,37} are fairly well established. On the other hand, neither the electron-band velocity at

the Fermi surface nor the electron-phonon matrix element for small and intermediate q values were previously known to sufficient accuracy to carry out accurate calculations. We have proposed on the basis of both theory and experiment a modification of the Stark and Falicov nonlocal pseudopotential which retains the same Fermi surface but alters the band velocity and the pseudopotential for small and intermediate values of q . We believe that this model gives fairly accurate results for electron-phonon effects. It produces a quasi-particle velocity which is in good agreement with Rahn and Sabo,⁵⁰ gives cyclotron resonance masses in good agreement with all orbits of Brookbanks⁶² and with all but a few orbits of Sabo,⁴⁹ and produces an anisotropy of the superconducting energy gap which agrees well with Cleavelin and Marshall.⁵⁷ Unfortunately, the results of this model do not agree with the Fermi-surface velocity measurements of Rowell,⁵¹ with the cyclotron mass of Sabo⁴⁹ for the crucial lens central orbits for H near the c axis, or with the superconducting ultrasonic-attenuation measurements of Dobbs *et al.*,⁵⁸ but neither do the measurements of Rahn and Sabo,⁵⁰ of Brookbanks,⁶² or of Cleavelin and Marshall⁵⁷ agree with these.

ACKNOWLEDGMENTS

This research was supported in part by NSF Grants No. DMR 73-07590 and No. DMR 77-10549. We wish to thank Professor G. Gilat for sending us his table of the energy-wave-number characteristic, Dr. D. Parsons for lending us a copy of Brookbanks' thesis, and Dr. P. B. Allen, Dr. J. P. Carbotte, Dr. J. A. Moriarty, Dr. R. W. Stark, and Dr. W. J. Tomasz for valuable conversations. One of us (J. C. S.) is grateful for the hospitality of Professor A. B. Pippard at the Cavendish Laboratory, Cambridge and of Professor K. H. Benne-

mann at the Free University of Berlin during stays when part of this paper was written.

APPENDIX

We are able to use a simplified model to understand the discontinuity in $\lambda_{\vec{k}}$ across certain Bragg planes. We consider a Fermi surface which is spherical except for small distortions near two symmetrically located Bragg planes. The limiting pseudo-wave-functions for states at \vec{k}_1 and \vec{k}_2 are, respectively, given by

$$|X_{\vec{k}_1}^+\rangle = (2)^{-1/2}(|\vec{k}_1\rangle + |\vec{k}_1 + \vec{G}\rangle), \quad (\text{A1})$$

$$|X_{\vec{k}_2}^+\rangle = (2)^{-1/2}(|\vec{k}_2\rangle - |\vec{k}_2 + \vec{G}\rangle), \quad (\text{A2})$$

where \vec{k}_1 and \vec{k}_2 are located on opposite sides of one of the Bragg planes. Assuming we may approximate all final states by their single-OPW value, we have for the matrix elements

$$g_{\vec{k}, \vec{k}_1}^+ \lambda = (2)^{-1/2}(g_{\vec{k}, \vec{k}_1}^+ \lambda + g_{\vec{k}, \vec{k}_1 + \vec{G}}^+ \lambda), \quad (\text{A3})$$

$$g_{\vec{k}, \vec{k}_2}^+ \lambda = (2)^{-1/2}(g_{\vec{k}, \vec{k}_2}^+ \lambda - g_{\vec{k}, \vec{k}_2 + \vec{G}}^+ \lambda). \quad (\text{A4})$$

Since the Fermi-surface distortions are small, we may approximate

$$g_{\vec{k}, \vec{k}_1}^+ \lambda \approx g_{\vec{k}, \vec{k}_2}^+ \lambda, \quad (\text{A5})$$

$$g_{\vec{k}, \vec{k}_1 + \vec{G}}^+ \lambda \approx g_{\vec{k}, \vec{k}_2 + \vec{G}}^+ \lambda. \quad (\text{A6})$$

Inserting these into Eq. (30) we obtain

$$\alpha^2 F(\vec{k}_1, \omega) = [\frac{1}{2}\alpha_0^2(\omega) + \frac{1}{2}\alpha_G^2(\omega) + \alpha_0^2(\omega)\alpha_G(\omega)]F(\omega), \quad (\text{A7})$$

$$\alpha^2 F(\vec{k}_2, \omega) = [\frac{1}{2}\alpha_0^2(\omega) + \frac{1}{2}\alpha_G^2(\omega) - \alpha_0^2(\omega)\alpha_G(\omega)]F(\omega) \quad (\text{A8})$$

where one merely has to identify the cross term in $|g_{\vec{k}, \vec{k}_i}^+ \lambda|^2$ to obtain the three terms in brackets. By symmetry, $\alpha_0^2(\omega) = \alpha_G^2(\omega)$ equals the single-OPW result. Thus we have a discontinuity of $2|\alpha_0^2(\omega)\alpha_G(\omega)|F(\omega)$, which is, in general, less than $2\alpha_0^2 F(\omega)$.

*Based in part on the Ph.D. thesis of P. G. T., Indiana University.

†Present address: Decision Science Applications, Inc., 1401 Wilson Blvd., Arlington, Va.

¹Preliminary results of this calculation were presented at the Thirteenth International Conference on Low Temperature Physics, Boulder, 1972; P. G. Tomlinson and J. C. Swihart, in *Low Temperature Physics*, edited by K. D. Timmerhaus, W. J. O'Sullivan, and E. F. Hammel (Plenum, New York, 1974), Vol. 4, p. 269.

²P. G. Tomlinson, following paper, Phys. Rev. B **19**, 1893 (1979); P. G. Tomlinson, and J. C. Swihart, Phys. Condens. Matter **19**, 117 (1975).

³J. C. Swihart, D. J. Scalapino, and Y. Wada, in *Low Temperature Physics LT-9*, edited by J. G. Daunt,

D. O. Edwards, F. J. Milford, and M. Yaqub (Plenum, New York, 1965), p. 607; Phys. Rev. Lett. **14**, 106 (1965).

⁴N. W. Ashcroft and J. W. Wilkins, Phys. Lett. **14**, 285 (1965).

⁵D. J. Scalapino, Y. Wada, and J. C. Swihart, Phys. Rev. Lett. **14**, 102 (1965).

⁶P. Morel and P. W. Anderson, Phys. Rev. **125**, 1263 (1962).

⁷J. P. Carbotte and R. C. Dynes, Phys. Rev. **172**, 476 (1968).

⁸P. B. Allen and M. L. Cohen, Phys. Rev. **187**, 525 (1969); P. B. Allen, M. L. Cohen, L. M. Falicov, and R. V. Kasowski, Phys. Rev. Lett. **21**, 1794 (1968).

⁹J. F. Balsley and J. C. Swihart, in *Low Temperature*

- Physics LT-12*, edited by E. Kanda (Academic Press of Japan, Tokyo, 1971), p. 303; J. F. Balsley, Ph.D. thesis (Indiana Univ., Bloomington, 1969) (unpublished).
- ¹⁰C. R. Leavens and J. P. Carbotte, *Ann. Phys.* **70**, 338 (1972).
- ¹¹H. K. Leung, Ph.D. thesis (McMaster Univ., Hamilton, Ontario, 1974) (unpublished).
- ¹²A. B. Meador and W. E. Lawrence, *Phys. Rev. B* **15**, 1850 (1977).
- ¹³T. M. Rice and L. J. Sham, *Phys. Rev. B* **1**, 4546 (1970).
- ¹⁴P. T. Truant and J. P. Carbotte, *Can. J. Phys.* **51**, 922 (1973).
- ¹⁵P. T. Truant and J. P. Carbotte, *Phys. Rev. B* **6**, 3642 (1972).
- ¹⁶P. Pecheur and G. Toussaint, *Phys. Rev. B* **7**, 1223 (1973); *J. Phys. Chem. Solids* **33**, 2281 (1972).
- ¹⁷E. Borch, S. De Gennaro, and P. L. Tasselli, *Phys. Status Solidi B* **46**, 489 (1971).
- ¹⁸A. J. Bennett, *Phys. Rev.* **140**, A1902 (1965).
- ¹⁹P. G. Klemens, C. Van Baarle, and F. W. Gorter, *Physica* **30**, 1470 (1964).
- ²⁰N. W. Ashcroft and W. E. Lawrence, *Phys. Rev.* **175**, 938 (1968).
- ²¹R. W. Stark and L. M. Falicov, *Phys. Rev. Lett.* **19**, 795 (1967).
- ²²A. E. O. Animalu and V. Heine, *Philos. Mag.* **12**, 1249 (1965).
- ²³L. Almqvist and R. Stedman, *J. Phys. F* **1**, 785 (1971).
- ²⁴S. Auluck, *J. Low Temp. Phys.* **12**, 601 (1973).
- ²⁵R. W. Stark and S. Auluck (unpublished).
- ²⁶D. Nowak, *Phys. Rev. B* **6**, 3691 (1972).
- ²⁷S. G. Das, *Phys. Rev. B* **7**, 2238 (1973).
- ²⁸N. Chesser and J. D. Axe, *Phys. Rev. B* **9**, 4060 (1974).
- ²⁹W. A. Harrison, *Pseudopotentials in the Theory of Metals* (Benjamin, New York, 1966).
- ³⁰R. W. Shaw, Jr., *J. Phys. C* **2**, 2335 (1969); *Phys. Rev.* **174**, 769 (1968).
- ³¹G. Gilat, G. Rizzi, and G. Cubiotti, *Phys. Rev.* **185**, 971 (1969).
- ³²E. W. Kellermann, *Philos. Trans. R. Soc. A* **238**, 513 (1940).
- ³³E. G. Brovman, YuKagan, and A. Kholas, *Fiz. Tverd. Tela* **11**, 896 (1969) [*Sov. Phys. Solid State* **11**, 733 (1969)].
- ³⁴R. E. De Wames, T. Wolfram, and G. W. Lehman, *Phys. Rev.* **138**, A717 (1965).
- ³⁵F. M. Mueller, J. W. Garland, M. H. Cohen, and K. H. Bennemann, Argonne National Laboratory Report, 1969 (unpublished).
- ³⁶L. J. Sham, *Proc. Phys. Soc. Lond.* **78**, 895 (1961).
- ³⁷O. L. Steenhaut and R. G. Goodrich, *Phys. Rev. B* **1**, 4511 (1970).
- ³⁸F. Herman and S. Skillman, *Atomic Structure Calculations* (Prentice-Hall, Englewood Cliffs, N. J., 1965).
- ³⁹W. L. McMillan, *Phys. Rev.* **167**, 331 (1968).
- ⁴⁰J. C. Holste, *Phys. Rev. B* **6**, 2495 (1972).
- ⁴¹R. E. Fasnacht and J. R. Dillinger, *Phys. Rev.* **164**, 569 (1967).
- ⁴²J. A. Moriarty, *Phys. Rev. B* **10**, 3075 (1974); private communication.
- ⁴³R. W. Shaw, Jr., *J. Phys. C* **2**, 2350 (1969).
- ⁴⁴M. Appapillai and A. R. Williams, *J. Phys. F* **3**, 759 (1973).
- ⁴⁵W. L. McMillan and J. M. Rowell, in *Superconductivity*, edited by R. D. Parks (Marcel Dekker, New York, 1969), Vol. 1, p. 561.
- ⁴⁶D. J. Scalapino, in Ref. 45, p. 449.
- ⁴⁷E. E. Havinga, *Phys. Lett. A* **26**, 244 (1968).
- ⁴⁸L. J. Sham and J. M. Ziman, in *Solid State Physics*, edited by F. Seitz and D. Turnbull (Academic, New York, 1963), Vol. 15, p. 223.
- ⁴⁹J. J. Sabo, Jr., *Phys. Rev. B* **1**, 1479 (1970).
- ⁵⁰J. P. Rahn and J. J. Sabo, Jr., *Phys. Rev. B* **6**, 3666 (1972).
- ⁵¹J. M. Rowell, *Phys. Rev. Lett.* **30**, 167 (1973); *J. Vac. Sci. Technol.* **10**, 702 (1973).
- ⁵²S. L. Colucci, W. J. Tomasch, and H. J. Lee, *Phys. Rev. Lett.* **32**, 590 (1974).
- ⁵³T. Wolfram, *Phys. Rev.* **170**, 481 (1968).
- ⁵⁴P. T. Truant and J. P. Carbotte, *J. Low Temp. Phys.* **12**, 31 (1973).
- ⁵⁵G. B. Donaldson, *Proceedings of LT-10*, edited by M. P. Malkov (VINITI, Moscow, 1967), Vol. IIB, p. 291.
- ⁵⁶J. W. Garland, K. H. Bennemann, and F. M. Mueller, *Phys. Rev. Lett.* **21**, 1315 (1968).
- ⁵⁷C. R. Cleavelin and B. J. Marshall, *Phys. Rev. B* **10**, 1902 (1974).
- ⁵⁸E. R. Dobbs, M. J. Lea, and D. R. Peck, *Proc. R. Soc. A* **334**, 379 (1973).
- ⁵⁹E. Ducla-Soares and J. D. N. Cheeke, in *Low Temperature Physics LT-12*, edited by E. Kanda (Academic Press of Japan, Tokyo, 1970), p. 305.
- ⁶⁰N. V. Zavaritskii, *Zh. Eksp. Teor. Fiz.* **39**, 1193 (1960) [*Sov. Phys. JETP* **12**, 831 (1961)].
- ⁶¹J. B. Evans, M. P. Garfunkel, and D. A. Hayes, *Phys. Rev. B* **1**, 3629 (1970); D. A. Hayes, *ibid.* **1**, 3631 (1970).
- ⁶²D. M. Brookbanks, *J. Phys. F* **3**, 988 (1973).
- ⁶³P. B. Allen and R. C. Dynes, *Phys. Rev.*, **B 12**, 905 (1975).